NUMERICAL SIMULATION OF TRANSVERSE FUEL INJECTION

Marlon Mao and David W. Riggins,
Analytical Services and Materials, Inc.
Hampton, VA 23666

Charles R. McClinton
NASA Langley Research Center
Hampton, VA 23665

ABSTRACT

This paper presents a review of recent work at NASA-LaRC to compare the predictions of transverse fuel injector flow fields and mixing performance with experimental results. Various "cold" (non-reactive) mixing studies have been selected for code calibration; these include the effects of boundary layer thickness and injection angle for sonic hydrogen injection into supersonic air. Angled injection of helium is also included. This study was performed using both the three-dimensional elliptic and the parabolized Navier-Stokes (PNS) versions of SPARK. Axial solution planes were passed from PNS to elliptic and elliptic to PNS in order to efficiently generate solutions. The PNS version is used both upstream and far downstream of the injector where the flow can be considered parabolic in nature. The comparisons are used to identify experimental deficiencies and computational procedures to improve agreement.

NOMENCLATURE

$A_{\alpha=0}$	area enclosed by the $\alpha = 0$ curve
D	injector diameter
$\dot{m}_{H_2,inj}$	mass flow rate of injected H_2
$\dot{m}_{H_2,mix}$	mass flow rate of mixed H_2
$\dot{m}_{H_2,total}$	total H_2 mass flow rate from flow field integration
M	Mach number
p	pressure
p_t	total pressure
P	penetration to outer edge of mixing region (height of $\alpha_{H_2} = .00035$ or $x_{He} = .005$ contour)
$\bar{q}$	jet-to-air dynamic pressure ratio
Re	Reynolds number
Sc_t	turbulent Schmidt number
T	temperature
T_t	total temperature
T_w	plate temperature
u	axial velocity
W	width
x or X	axial coordinate
x_{He}	helium mole fraction

y *or* Y	lateral coordinate
z *or* Z	coordinate normal to plate
Z_m	height of α_{max} contour
α	mass fraction
α_{max}	maximum mass fraction
α_R	mass fraction defined by Eqn. 1
α_s	stochiometric hydrogen mass fraction (0.0285)
β	air mass fraction (1-α)
δ	boundary layer thickness
η_m	mixing efficiency
η_m'	mixing efficiency with α_s = 0.01425
$(\eta_m')_{adj}$	mixing efficiency with α_s = 0.01425 and assuming missing fuel to be unmixed
ρ	density
θ_{inj}	injection angle

INTRODUCTION

Efficient hypersonic flight at speeds above Mach 6 require the use of supersonic combustion ramjet or scramjet engines. Research efforts to establish a technology base for scramjet engine components have been underway at NASA Langley Research Center (LaRC) since the mid 1960's. This research was focused on the Mach 4 to 7 speed range, the range within the enthalpy limits of combustion heated or arc heated facilities, and directed toward the inlet and combustor components of the engine. Combustor technology development[Ref. 1] was directed at understanding the requirements for and performance of fuel injection, mixing and reaction (ignition and flame holding) in the scramjet combustor environment, and incorporated a dual approach of experimental and computational technology development.

Experimental combustor technology development started with single[2-4] and multiple[5-7] fuel injector studies in cold flow to characterize fuel mixing, followed by reacting coaxial flow configurations[8,9] to characterize the supersonic combustion phenomena. Direct connect combustor experiments[10-16] were used to verify empirical models[17] for the mixing limited supersonic combustion process developed from the early mixing studies. Finally, the empirical combustor models were integrated into a complete subscale engine design and tested[18] over the Mach 4 to 7 speed range in two engine test facilities.

Computational fluid dynamics (CFD) technology development started with codes which contained the physical modeling necessary to predict the supersonic, chemically reacting flow encountered in a scramjet combustor[19]. Because of computer memory limitations, these codes were limited to two-dimensional or axisymmetric cases until the mid 1980's. The two-dimensional codes were calibrated to appropriate data for non-reacting fuel injection and mixing[20], and reacting fuel injection and mixing[21,22] in ducted flows. Various finite-rate chemistry models were developed and applied for hydrogen fuel[19,23] and silane-hydrogen-air mixtures[24]. Recent code applications have evaluated non-reactive three-dimensional fuel mixing[25] and reactive fuel mixing in confined simulated combustor flows[25-29]. Even though they have provided significant insight into these highly complex flow fields, these studies have not provided the essential features of code calibration for scramjet fuel mixing.

The objective of this paper is to present comparisons of numerical predictions with experimental measurements for non-reacting fuel injection into a supersonic freestream and to document efforts to improve the agreement. This study will look at a large data set with the intent of identifying experimental limitations and correct procedures to use when exercising the codes. The primary index of agreement is overall mixing efficiency of the fuel or simulated fuel. In the absence of experimental mixing efficiency, the index defaults to fuel mass or mole fraction distributions. Secondary values of interest include fuel penetration and spreading, wall pressure, and any other measured data available.

A brief description of the experimental tests chosen for this paper is followed by a brief description of the SPARK codes. The computational method used to solve the injection problems is discussed along with convergence criteria for the elliptic region. The grid and boundary conditions are also given. Results from the calculations are then compared with data in order to demonstrate the accuracy of the numerical modeling.

EXPERIMENTAL CONFIGURATION

Details of the flat plate non-reacting injection cases modeled are provided in Table 1. Variables in the table include the jet-to-air dynamic pressure ratio, $\bar{q}$; the freestream Mach number, M_{air}; freestream Reynolds number, Re; downstream injection angle, θ_{inj}, measured from the plate surface; the boundary-layer thickness upstream of the injector normalized by jet diameter, δ/D; and the jet diameter in centimeters, D.

Table 1. Summary of Conditions

Case	Injectant	$\bar{q}$	M_{air}	Re(m^{-1})	θ_{inj}	δ/D	D(cm)	Ref.
1	hydrogen	1.0	4.05	$8.3\text{x}10^8$	90^o	1.25	0.2540	4
2	hydrogen	1.0	4.05	$6.19\text{x}10^7$	90^o	2.51	0.1016	3
3	hydrogen	1.0	4.05	$8.0\text{x}10^8$	90^o	6.25	0.0508	4
4	hydrogen	1.0	4.05	$6.19\text{x}10^7$	30^o	3.40	0.1016	7
5	helium	0.6	3.00	$5.2\text{x}10^7$	30^o	2.20	0.3175	30
6	helium	3.1	3.00	$5.2\text{x}10^7$	30^o	2.20	0.3175	30
7	helium	0.27	3.00	$5.2\text{x}10^7$	15^o	2.20	0.3175	30

Table 2. Experimental Flow Properties

	Air			Injectant			
Case	p_t(MPa)	T_t(K)	Mach	Gas	p_t(MPa)	T_t(K)	Mach
1	1.72	295	4.05	H_2	0.33	289	1.0
2	1.38	294	4.05	H_2	0.27	294	1.0
3	1.72	303	4.05	H_2	0.32	298	1.0
4	1.38	300	4.05	H_2	0.27	295	1.0
5	.655	290	3.00	He	0.17	295	1.0
6	.655	290	3.00	He	0.86	295	1.0
7	.655	290	3.00	He	0.076	295	1.0

Cases 1-4 are from tests performed on a flat plate model (Fig. 1) in a Mach 4.05, 23x23 cm blow down tunnel. Table 2 presents nominal test conditions for the cold air and sonic

Flat-plate detail
(Dimensions are in cm)

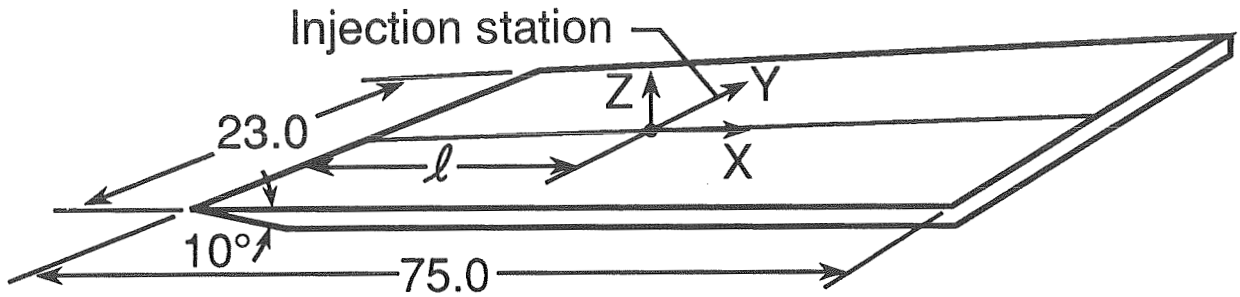

Injector detail
(Dimensions are in cm)

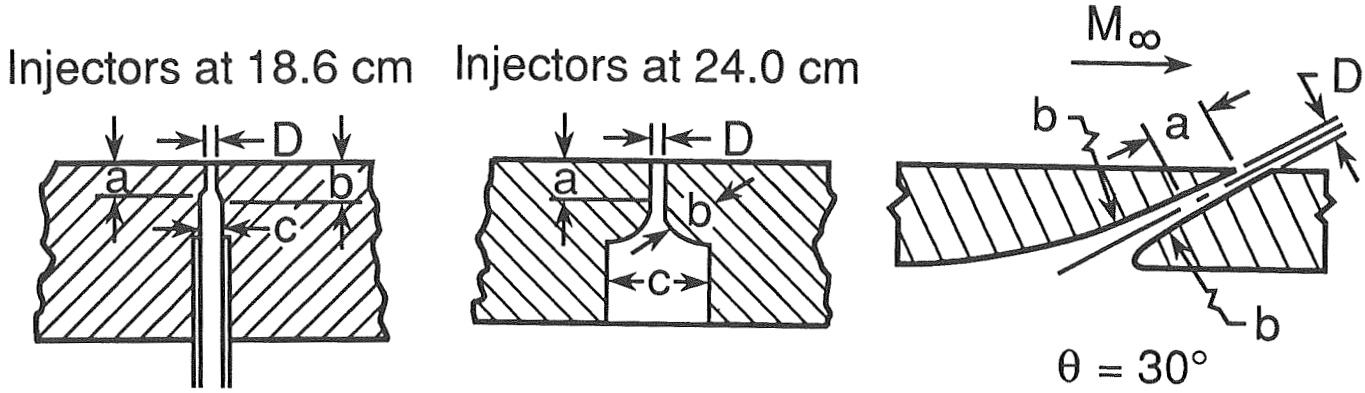

Case	ℓ	a	b	c	D	C_D
1 ref. 4	24.0	0.635	0.578	1.41	0.254	0.830
2 ref. 3	18.6	0.317	0.397	0.15	0.102	0.76
3 ref. 4	24.0	0.152	0.680	1.41	0.051	0.754
4 ref. 7	27.1	0.303	3.12	-	0.102	0.76

Figure 1. Experimental Model

hydrogen injectors. The facility was operated at stagnation pressures of either 1.38 or 1.72 MPa, but the four cases selected all operated with unity jet-to-freestream dynamic pressure ratio (see Table 1). Instrumentation was provided to measure the stagnation pressures and temperatures of hydrogen and air, plate-surface static pressures and hydrogen concentrations. In addition, the H_2 mass flow rate was measured using a sharp-edge orifice meter. Plate static-pressure orifices of 0.051 cm diameter were located on the longitudinal center line from 30D ahead of the injector station to 150D downstream for Case 4. In-stream measurements were made using a 0.038 cm ID pitot and a 0.102 cm OD conventional static probe. Gas samples were taken from the mixing region by the pitot probe and were analyzed with an on-line process gas chromatograph having a cycle time of 60 seconds.

Historically, mixing efficiency, η_m, is defined as that fraction of the least available reactant (i.e. O_2 or fuel) which would react if the fuel-air mixture were brought to chemical equilibrium without additional local or global mixing. Thus in fuel rich regions, all of the local oxygen is considered "mixed," while in fuel lean regions all of the fuel is mixed. Two definitions of mixing efficiency are required--one for flows which are globally fuel rich, and one for flows which are lean. For fuel lean flows, as those reported here,

$$\eta_m = \frac{\dot{m}_{H_2,mix}}{\dot{m}_{H_2,total}} = \frac{\int_{A_{\alpha=0}} \alpha_R \rho u dA}{\int_{A_{\alpha=0}} \alpha \rho u dA} \tag{1}$$

where: α is hydrogen (fuel) mass fraction

$$\alpha_R = \begin{cases} \alpha & where\ \alpha \le \alpha_s \\ \left(\frac{1-\alpha}{1-\alpha_s}\right)\alpha_s & where\ \alpha > \alpha_s \end{cases}$$

α_s is H_2 stochiometric mass fraction (0.0285)

$A_{\alpha=0}$ is the area enclosed by zero H_2 contour defining the extent of the mixing region

$\dot{m}_{H_2,mix}$ is mixed H_2 mass flow rate

$\dot{m}_{H_2,total}$ is total H_2 mass flow rate from flow field integration.

When $\alpha_{max} < \alpha_s$, η_m equals 1.0.

Experimental mixing efficiencies for the data from Ref. 3, 4 and 7 are determined by integration of the hydrogen and airflow contours as illustrated in Fig. 2. Overlaying the stochiometric fuel-air contour (α_s = 0.0285) on the H_2 and air flow contours to provide integration limits, the total hydrogen mixed and mixing efficiency are determined by the integration procedure of Eqn. 1. Total hydrogen mixed in the fuel lean region is determined by integration of hydrogen flow rate in that region (Fig. 2b), while hydrogen mixed in the fuel rich region is determined by integration of the air flow rate within the fuel rich region (Fig. 2c).

As discussed in Ref. 3, one indication of the overall accuracy of the profile data is comparison of the integrated hydrogen mass flow rate with the metered hydrogen mass flow supplied to the jet. Figure 3 illustrates this comparison for all data in Ref. 3. Agreement of the integrated and metered mass flows improves as X/D increases and $\bar{q}$ decreases. This improvement is probably due to the smaller gradients in the concentration and velocity which are associated with the local turbulence level at the downstream stations and lower values of $\bar{q}$. It has also been suggested that selective sampling by the subcritical pitot probe produces the low indicated hydrogen composition[30].

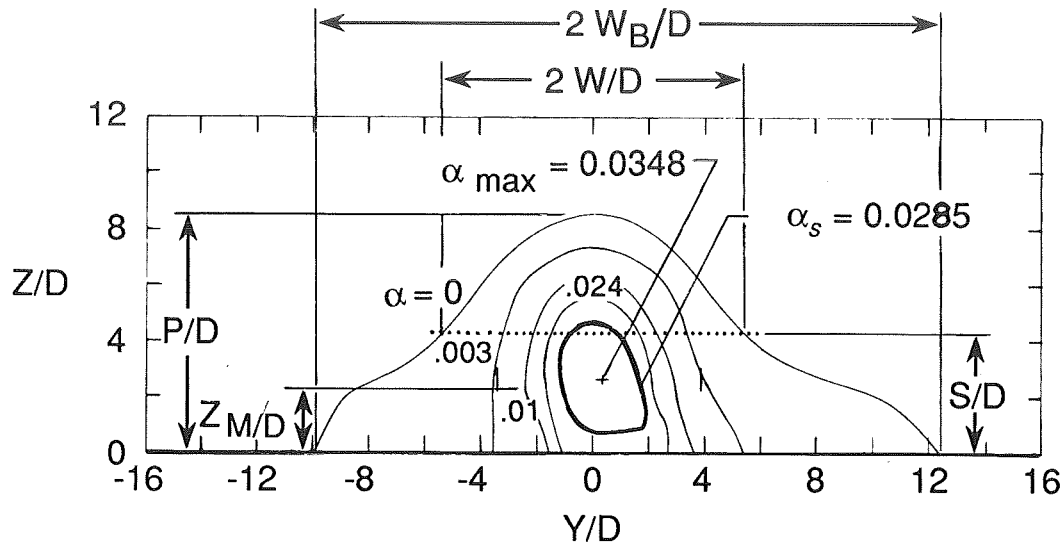

Hydrogen concentration contour

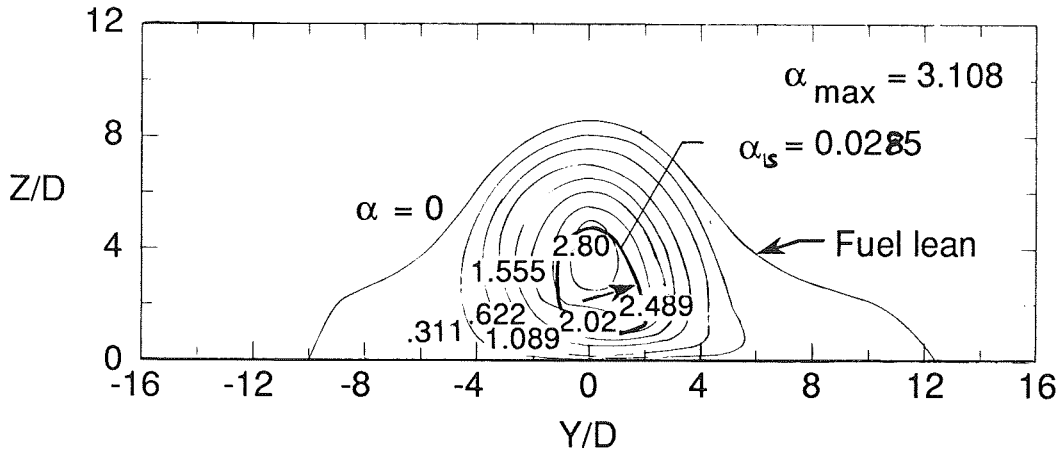

Hydrogen flow rate contours in kg/m^2-sec

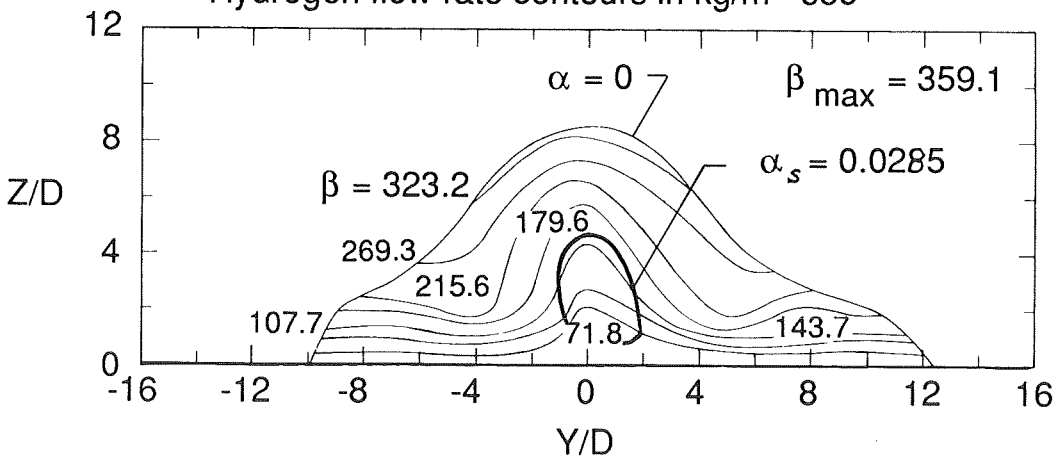

Airflow rate contours in kg/m^2-sec

Figure 2. Experimental Determination of Mixing Efficiency.

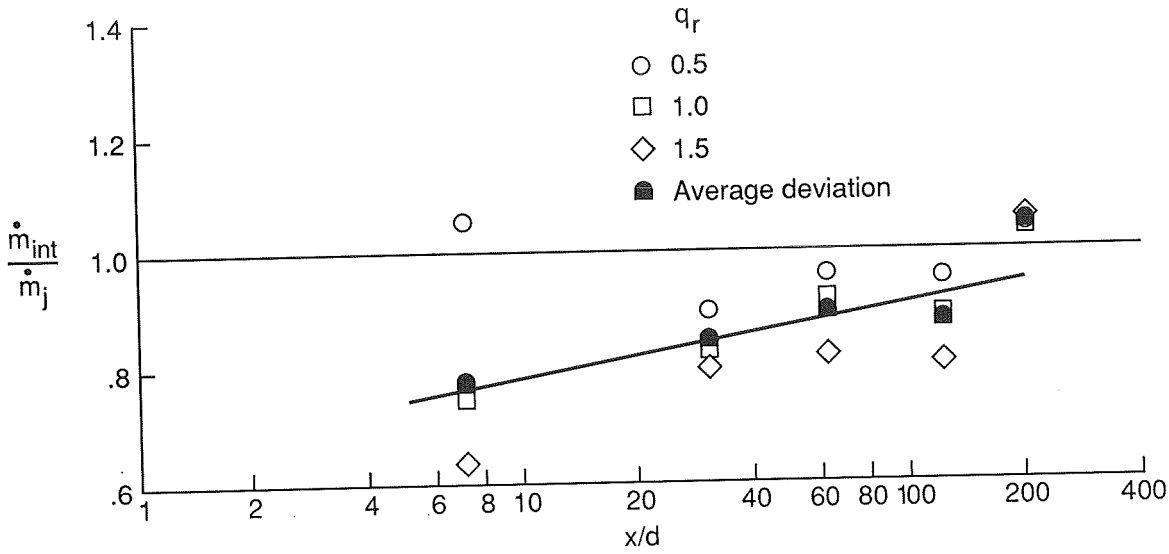

Figure 3. Results of Fuel Mass Flow Contour Integration [Ref. 3].

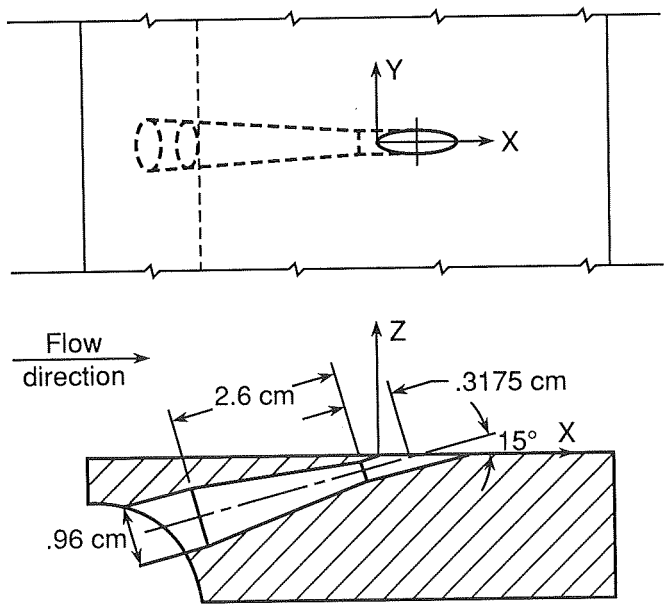

Figure 4. Schematic of 15^o Nozzle Design.

Cases 5-7 represent low-angled helium injection experiments performed in a Mach 3, 11x23 cm blow down tunnel at Virginia Tech[30] with injection from the lower tunnel wall. Boundary layer thickness at the fuel injector is about two jet diameters. Geometric details of the 15^o injector presented in Fig. 4 illustrate the converging and short 1-d constant diameter section used to provide the sonic helium jet. Nominal test conditions for the cold air and sonic helium injector are presented in Table 2. The facility is operated at a total pressure and temperature of 0.655±.02 MPa and 290 K respectively and helium is injected either at matched or underexpanded pressure. Instream measurements of fuel concentration, flow temperature, pitot and static pressure were obtained at axial stations of 20, 40 and 90 jet diameters downstream of the injector on the jet centerline. Additional surveys of fuel concentration were obtained at off jet centerline locations. The gas sampling probe[31] utilizes a very small internal expansion tip with an internal diameter of 0.028 cm (one tenth the injector diameter), which has sufficient internal expansion and flow suction to swallow the tip shock wave.

DESCRIPTION OF CODES

The LaRC SPARK family of CFD codes was used in this study. The two-dimensional Navier-Stokes code was originally developed and extensively validated for chemically reacting and mixing flows by Drummond[32] and has been expanded to three dimensions and validated by Carpenter[33]; this three-dimensional version has additionally been developed into a parabolized Navier-Stokes (PNS) version by Kamath[34]. The elliptic SPARK code can use either a temporally explicit second-order accurate MacCormack-based finite-difference technique to solve the mass, momentum, and energy conservation equations or a fourth-order compact spatial scheme[33] which provides high spatial accuracy and a convenient method for marching to the steady state. In addition, the code has the fourth-order time accurate Gottlieb scheme[33]. For mixing results, the source terms in the species continuity equations are set to zero.

At the time of this work, the SPARK codes contained only the Baldwin-Lomax algebraic turbulence model. The formulation used contained the constants as presented in the original paper[35] for a thin layer on a flat plate. Freestream turbulence in the tunnel was ignored. For Cases 5-7, the turbulent viscosity was limited to 1000 times the laminar viscosity. It was found in this investigation that the use of $Sc_t < 1.0$ enabled better agreement between numerical results and experimental data. There is both experimental and computational justification for the use of turbulent Schmidt numbers less than unity for flows such as that examined in this work[36,37].

SOLUTION METHODOLOGY

Due to limited computational resources, the solutions were performed in a piece-wise elliptic/PNS fashion. The flowfield upstream of the elliptic injection region is modeled using the SPARKPNS code in 2-d mode. The injection nearfield region, which is highly three-dimensional and characterized by such features as large-scale vorticity, separation ahead of and behind the injector, strong shocks and expansions, was computed with the 3-d elliptic version of the SPARK code. The injection region extended from six to ten jet diameters ahead of the injector to ten to forty jet diameters downstream of the injector, depending on the case. The 3-d SPARKPNS code was used in the farfield with the outflow plane from the elliptic code passed as a fixed inflow into the PNS code. A small inconsistency is inherent in this strategy which is illustrated in Fig. 5, since the character of the governing equations is changed discontinuously from the full Navier-Stokes (FNS) to that of the parabolized approximation. However, this was considered an acceptable compromise to achieve computational efficiency, and the inconsistency involved in the passing of a plane from the full Navier-Stokes elliptic domain to the parabolized version of these equations are believed to be small in

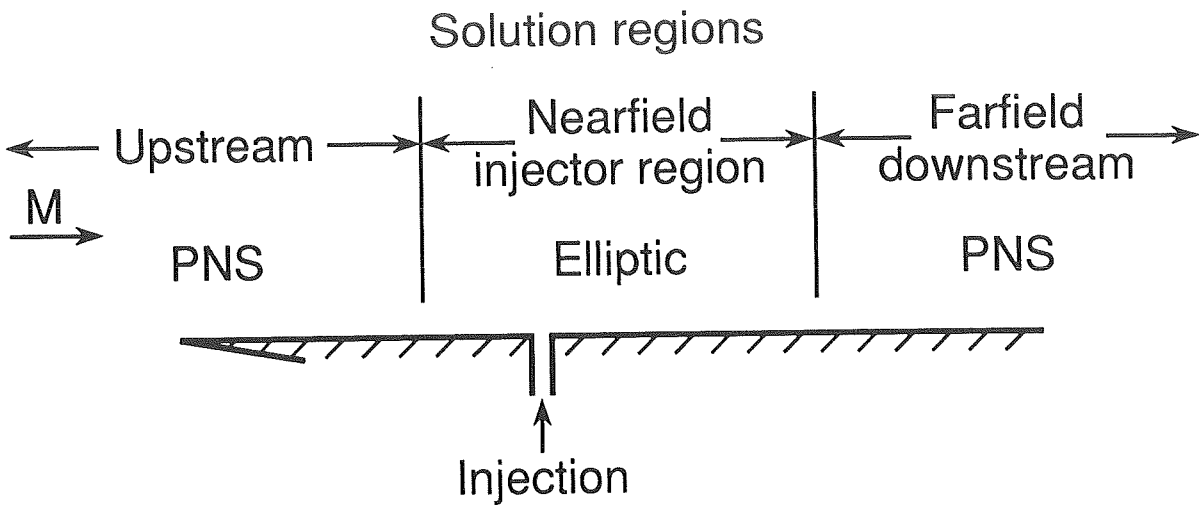

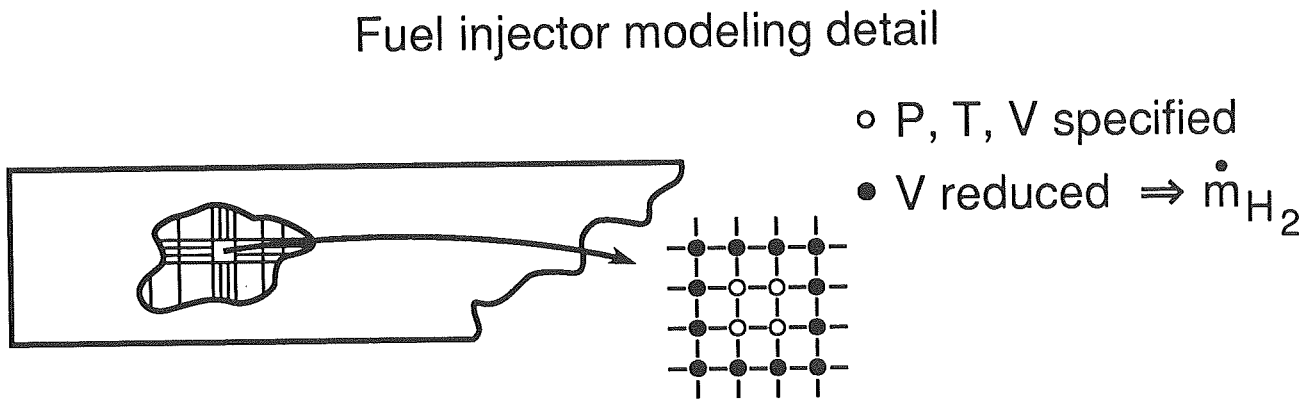

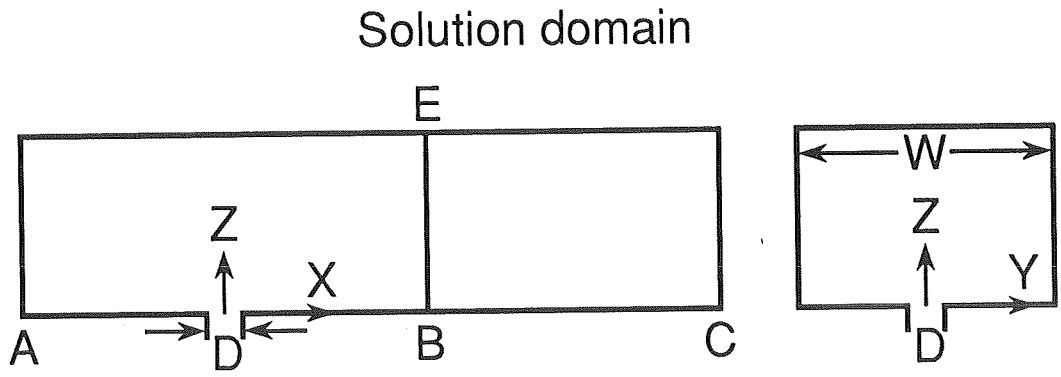

Figure 5. Solution Methodology

relation to turbulence and grid issues.

The computations presented here were performed on the Cray supercomputers of the Numerical Aerodynamic Simulation (NAS) at NASA Ames and the Cray 2 at LaRC. The mixing studies each took about 2-10 hours of CPU time. Convergence as defined in the next section occurred at about 10000 iterations. The parabolized computations in this study comprised about 15% of the CPU time used and a fraction of the memory.

CONVERGENCE REQUIREMENTS

Due to the swirling nature of the flow around and behind the injectors, the flow is at best quasi-steady, and there is some small fluctuation of pressure in the elliptic region as well as for flow parameters in the outflow plane passed to the parabolized code. Claimed convergence for an elliptic solution of this nature must be limited in its scope to the unchanging mean or averaged values of the parameters of interest such as density ($(\Delta\rho)_{max} < 5\%$) and the conservation (within 10%) of total fuel for all axial planes.

GRID AND BOUNDARY CONDITIONS

Grids for each solution discussed herein are summarized in Table 3. All cases used a rectangular grid for both the parabolic and elliptic regions with the downstream parabolic region having the same cross-sectional grid as in the elliptic. All meshes were clustered near the injector and near the plate. Grid domain represents the number of nodes in the axial, lateral and vertical directions. The last 5 columns in the table deal with grid dimensions in terms of jet diameter with the origin at the injector center (Fig. 5).

All inflow boundary values were fixed. No-slip boundary conditions were applied to the flat plate, which was either at a constant temperature or adiabatic. All of the circular injectors were modeled as rectangles on the mesh lower boundary (the plate). The nodes within the orifice had their properties set to the jet properties calculated from the stagnation properties listed in Table 2. The computational injector was modeled to match the injector area. The computational area and/or the velocity on the jet edge nodes were then reduced to match the metered injectant mass flow, thereby simulating a discharge coefficient due to losses near the injector walls. All other boundary planes were set as outflow planes, except for those of Case 4 which had multiple injectors and thus two symmetry planes. (Table 3 also lists the number of nodes used to model an injector. At each such node, the jet conditions were applied.)

Table 3. Grid and Solution Details

Case	Domain	Injector	Sc_t	T_w	A/D	B/D	C/D	E/D	W/D
1	41x61x41	25	0.2,0.5	250.	-6	10	120	16	32
	41x51x51	20	0.2	250.	-6	10	120	16	16
2	51x31x41	25	0.2,0.5,1.0	300.	-16	33	120	49	49
	51x31x21	25	0.2,0.5,1.0	300.	-16	33	120	49	49
	41x25x21	9	0.2,0.5,1.0	300.	-16	33	120	49	49
3	41x61x41	25	0.2	250.	-6	10	120	16	32
4	41x31x41	25	0.2	300.	-6	10	120	14	6.25
5	51x41x41	35	0.5	adia.	-6	10	90	16	16
6	51x41x41	35	0.5	adia.	-6	10	90	16	16
7	51x41x41	55	0.5	adia.	-6	10	90	16	16

RESULTS

This section presents computational results and comparisons with experimental data for the seven cases. The computational analysis was performed with several values of turbulent Schmidt number, and one case was evaluated using several mesh densities. Details of these variations are highlighted. The following section will discuss the implications of these findings and give recommendations on applying the SPARK or equivalent CFD codes to fuel injector problems.

Case 1

Computational results for Case 1 are presented in Figs. 6-9. Two different solutions were obtained: one with Sc_t = 0.2 and one with Sc_t = 0.5. Hydrogen concentration contours in the vertical X-Z plane through the jet centerline are given in Fig. 6 for the solution with Sc_t =0.2. These results illustrate fuel feeding upstream into a region of boundary layer separation, the penetration and dispersion of the hydrogen core in the nearfield, and penetration of the outer edge of the fuel. Note that the α = 0.10 contour (3.5 times stochiometric) extends about 3 jet diameters upstream of the injector centerline, and the .005 contour extends to about 4 jet diameters upstream. The hydrogen core (i.e. the region of highest concentration extending downstream from the initial jet, indicated by the dashed line in Fig. 6a) penetrates to about 1.2 jet diameters above the flat plate and the 0.40 contour (an arbitrarily selected indicator of core breakup) persists about 6.5D downstream. The peak hydrogen concentration moves back toward the plate and lies along the surface for axial stations past 10 diameters. Fig. 6b shows combined FNS and PNS results and indicates complete mixing by 80D downstream ($\alpha<\alpha_s$ everywhere).

Computational and experimental results are compared in Fig. 7 by lateral Y-Z plane hydrogen mass fraction contours at the 120D station. The outer edge of the fueled region is represented here by the 0.003 H_2 mass fraction contour. The computational results have greater penetration P/D (see Fig. 2a) and lateral spreading than experimental results with the spreading near the plate W_b/D nearly double that of the experiment. However, the computed 0.010 hydrogen mass fraction contour illustrates slightly (≈20%) lower penetration and slightly (≈25%) greater spreading than the experimental contour.

Computed vertical jet centerline profiles (Sc_t = 0.2) at the 120 jet diameter station are presented in Fig. 8 and compared with measured H_2 mass fraction, static pressure, static temperature and velocity. The profiles are in reasonable agreement, except for the location of the peak hydrogen concentration. The dashed curve represents results from a solution with Sc_t = 0.5 in both elliptic and parabolized solutions. Again, the peak concentration is adjacent to the wall, but the peak value is nearly double that measured because of reduced mass transport. However, penetration to the outer edge of the mixing region is not significantly affected by the value of Sc_t

Longitudinal variation in predicted fuel mixing efficiency is presented in Fig. 9 for both solutions discussed above. Mixing efficiency presented in this figure is **NOT** as defined in Eqn. 1. because of an error in the CFD code used for this and the other hydrogen cases. Mixing efficiency, η'_m, for Fig. 9 is defined by Eqn. 1, but with

$$\alpha_s = 0.01425 \tag{2}$$

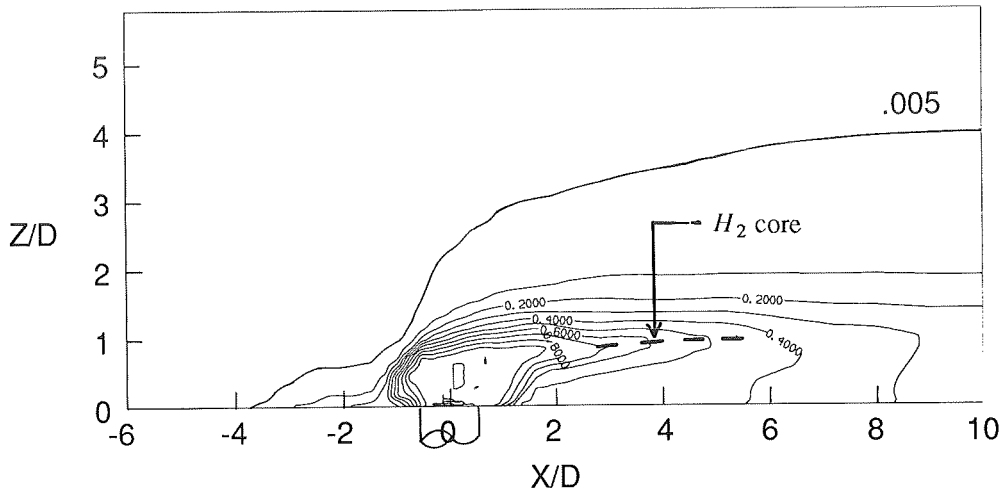

a) H_2 contours, elliptic region.

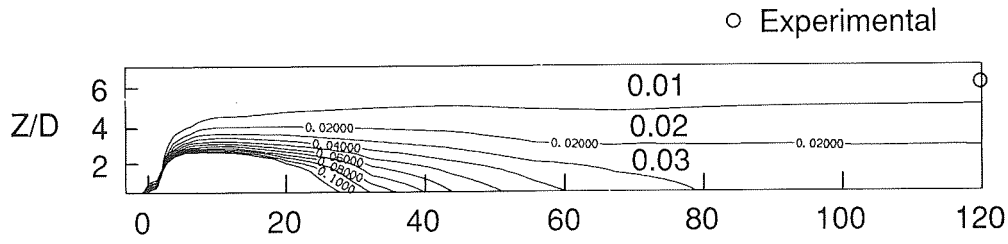

b) H_2 contours, elliptic plus PNS region.

Figure 6. Longitudinal Hydrogen Mass Fraction Contours; Case 1, Sc_t = 0.2.

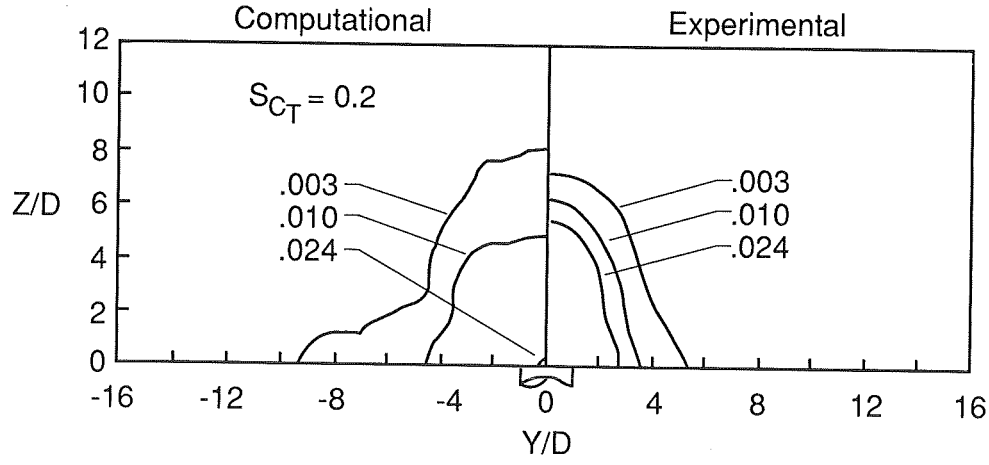

Figure 7. Lateral Hydrogen Distribution at X/D = 120; Case 1, Sc_t = 0.2.

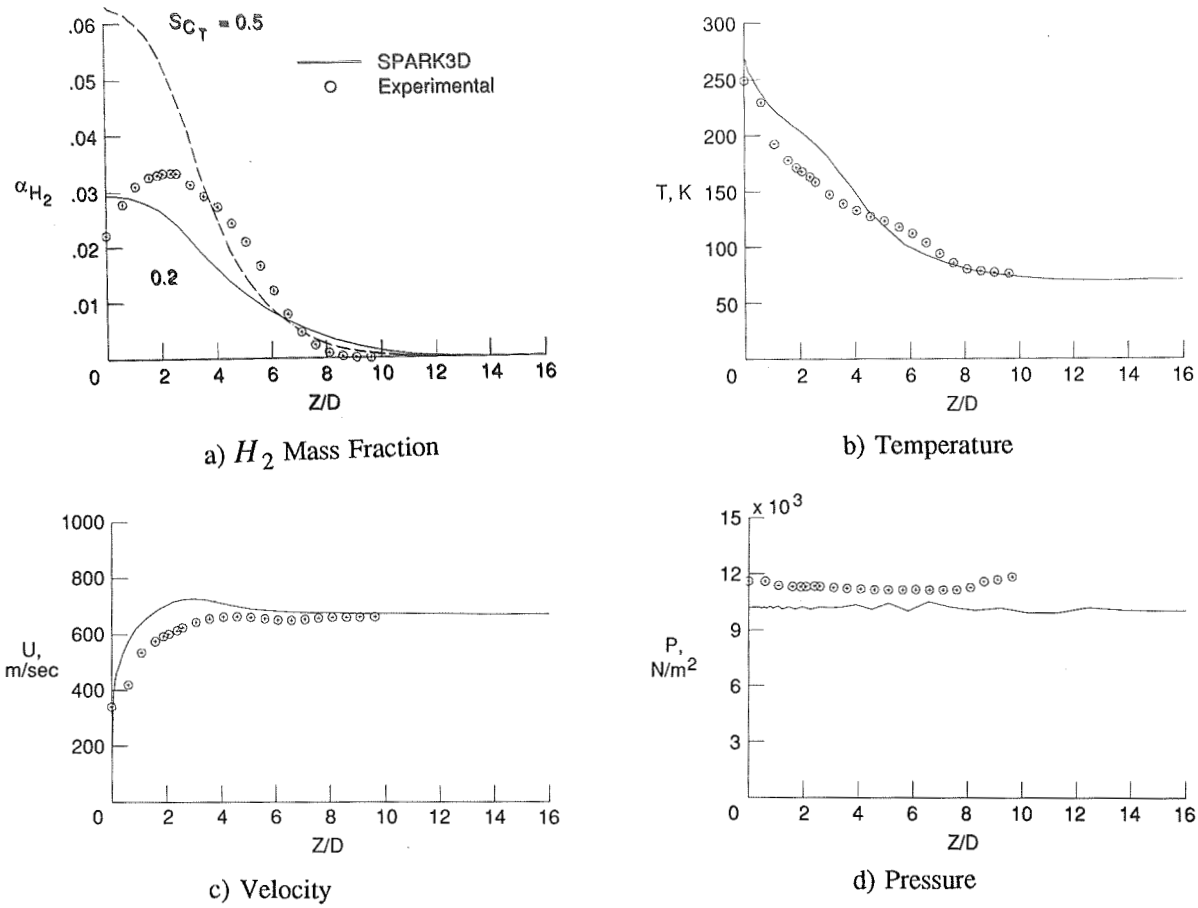

Figure 8. Vertical Centerline Profiles at X/D =120; Case 1, Sc_t = 0.2.

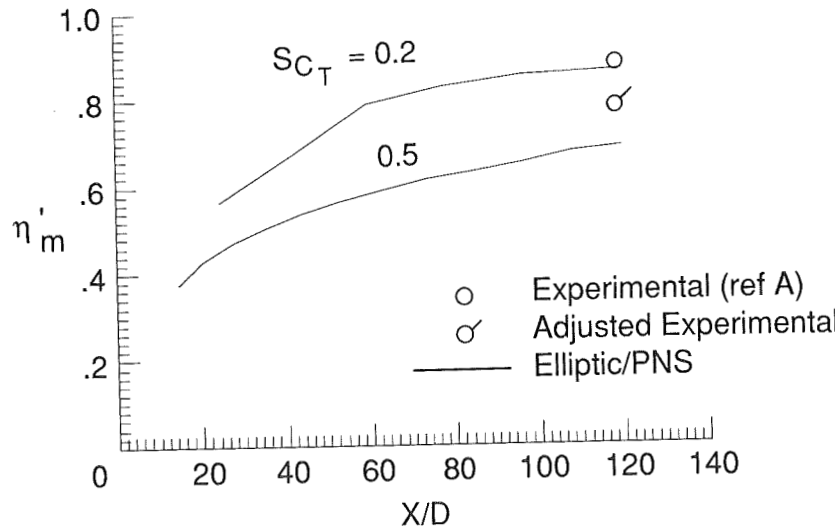

Figure 9. Fuel Mixing Efficiency Distribution; Case 1.

Experimental η'_m determined by integration of Ref. 4 contours at X/D = 120 is presented by unflagged symbol. Although this is not the standard definition, the comparison of experimental and computational results using this method provides a reasonable percent error in modeling mixing efficiency. For this case, between 10% to 20% of the injected fuel was not accounted for in the experimental downstream survey. The flagged symbol represents the mixing efficiency if all of the missing fuel is assumed to be unmixed; i.e.:

$$(\eta'_m)_{adj} = \int_{A_{\alpha=0}} \frac{\alpha_R \rho u dA}{\dot{m}_{H_2,inj}} \tag{3}$$

where α_s is defined by Eqn. 2. Computational results are in good agreement with experimental results when performed using Sc_t = 0.2 and with the adjusted experimental result when using Sc_t = 0.5. At the 120 diameter station, the calculated mixing efficiency for Sc_t = 0.5 is only 20% lower than for Sc_t = 0.2, whereas α_{max} is more than double for the Sc_t = 0.2 case. The use of an adjusted mixing efficiency results from concern about quality of this older data in light of good agreement with the newer He injection data for Cases 5-7. This adjusted mixing efficiency represents the lowest bound of experimental scatter conceivable to account for limitations.

Case 2

Ten computational solutions were obtained for Case 2 for three different values of the turbulent Schmidt number on three different density grids plus one laminar fine grid solution. Figures 10-13 illustrate flow details obtained with a fine grid and Sc_t of either 0.2 or 0.5. Figures 14-15 illustrate the sensitivity of mixing efficiency to various grids and Sc_t plus one laminar solution.

Hydrogen contours (Sc_t = 0.5) presented in Figs. 10a,b illustrate fuel penetration, decay of the core and details of the upstream flow separation. The 0.10 contour (3 times stochiometric) extends less than 1.5 jet diameters upstream of the jet centerline, and the .005 contour extends about 3.5 diameters upstream. The H_2 core penetrates about 2D, and the 0.40 contour persists about 6.2D downstream. Peak concentration moves back to the wall at about X/D = 25 (not shown). Comparison with experimental penetration of the 0.010 hydrogen mass fraction contour are within 10% at X/D = 7, 30, 60 and 120 (Fig. 10b).

Hydrogen contours (Sc_t = 0.5) presented in Fig. 10c illustrate fuel penetration, decay of the core and details of the upstream flow separation for the same jet with the same inflow plane including boundary layer profile, but with no turbulence in the elliptic region. As expected for a disturbed laminar flow, the upstream separation region has become quite extensive (It should be noted that this solution is not completely converged). The H_2 core penetrates about 2.3D, and the 0.40 contour persists about 8D downstream. Both of these values are slightly greater than for the turbulent solution.

Computed lateral spreading of the fuel at X/D at 120D is illustrated in Fig. 11 for each value of Sc_t for the fine mesh. At Z/D = 4.0, lateral spreading W/D (see Fig. 4) of all computational contours is greater than experimental values, and higher Sc_t produces less spreading. At Z/D = 0, lateral spreading W_b/D of all computational contours is in reasonable agreement with the experimental results. Fuel penetration (P/D) increases for the lowest value of Sc_t, but all cases exceed experimental results.

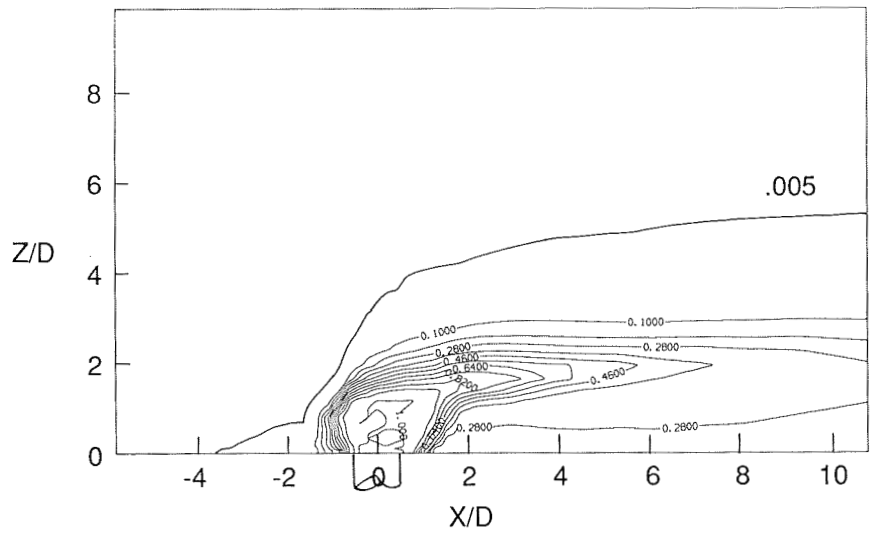

a) H_2 contours, elliptic region.

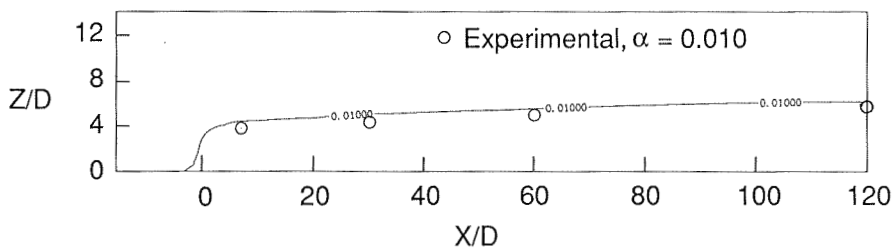

b) H_2 contours, elliptic plus PNS region.

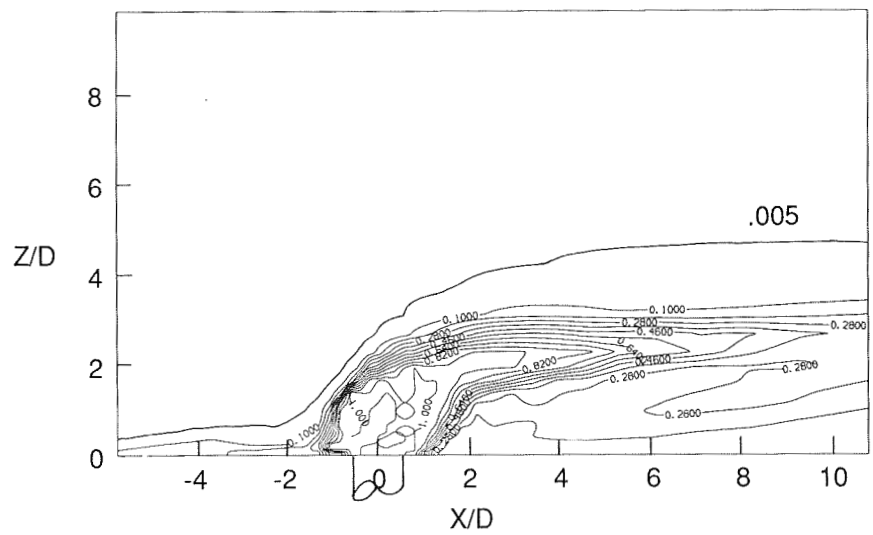

c) H_2 contours, elliptic region, Laminar Flow.

Figure 10. Longitudinal Hydrogen Mass Fraction Contours; Case 2, Sc_t = 0.5.

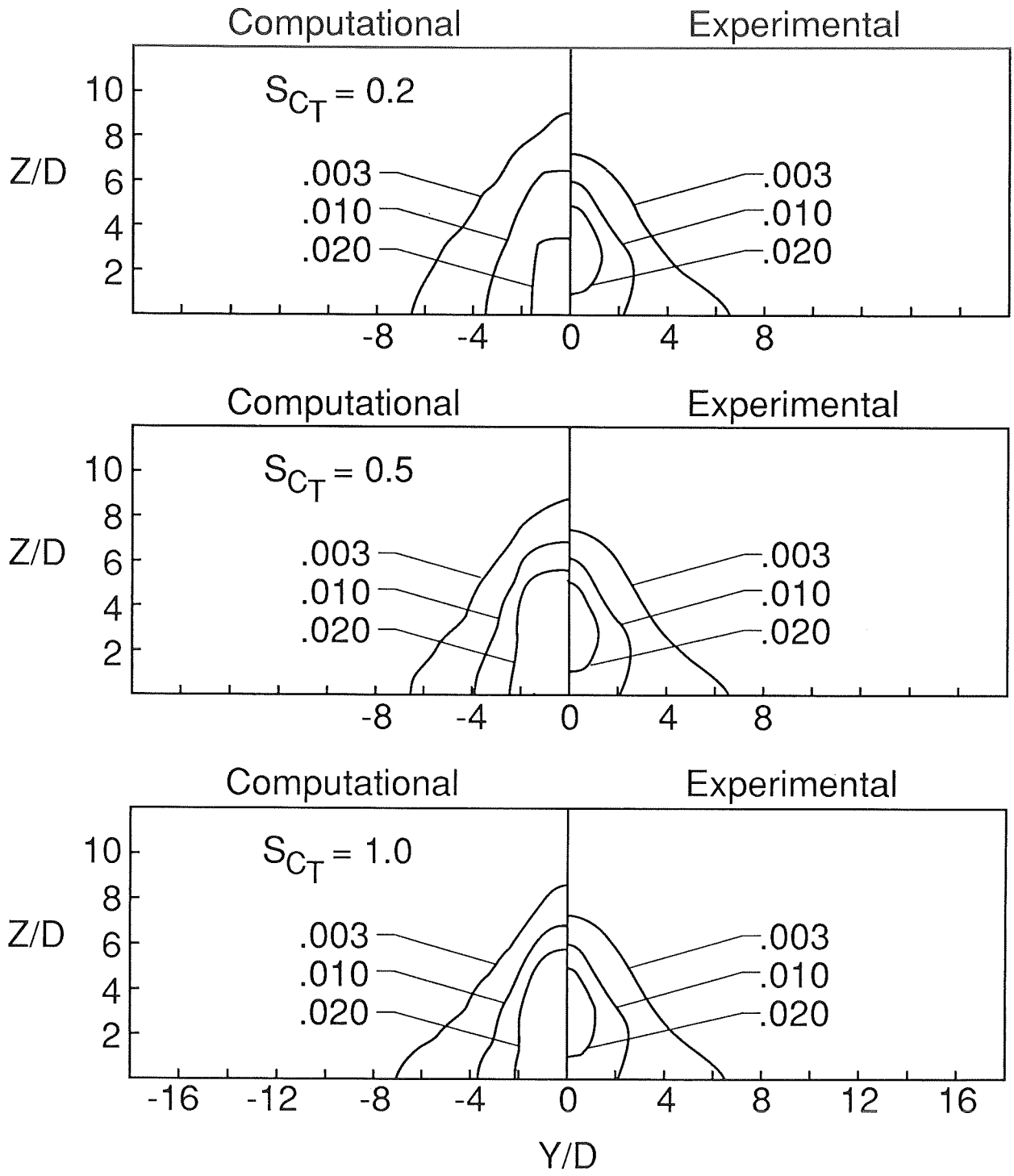

Figure 11. Lateral Hydrogen Distribution at X/D = 120; Case 2.

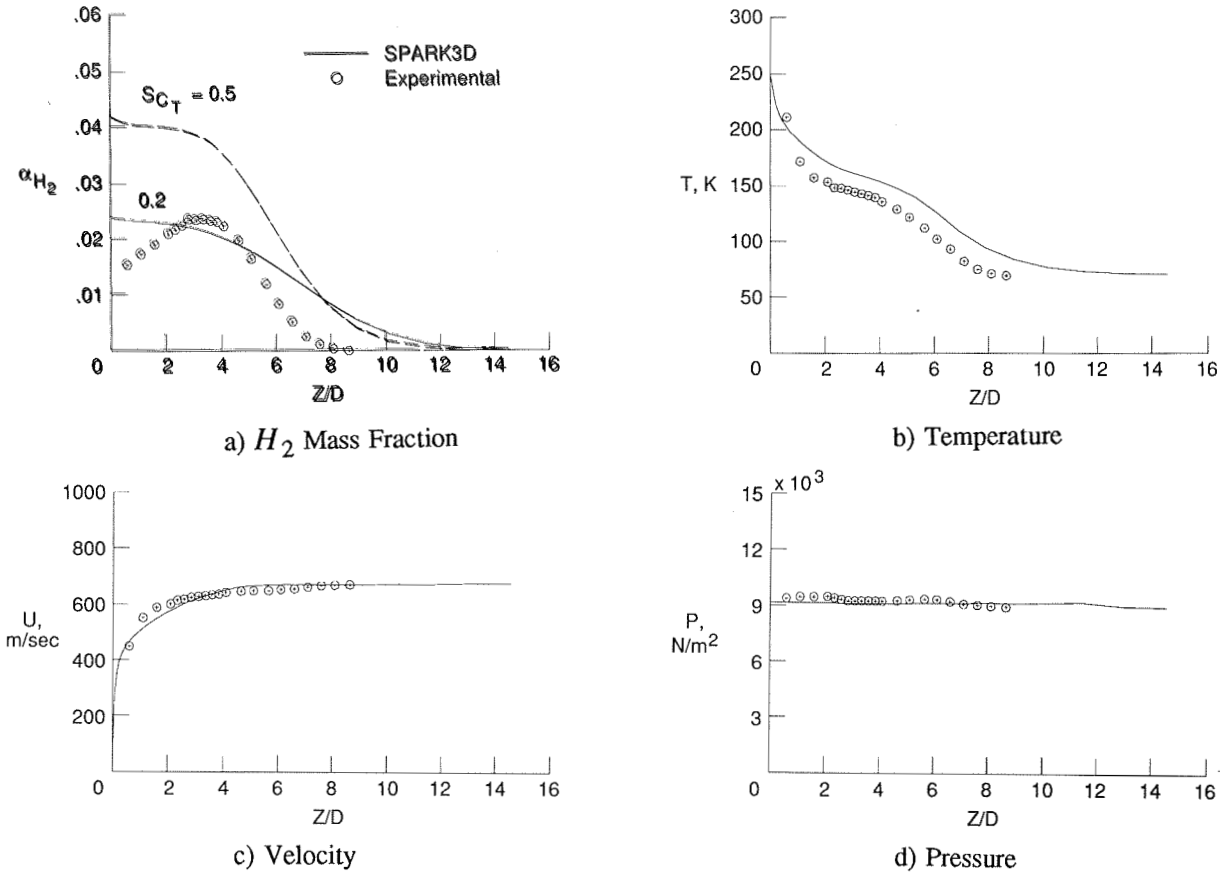

Figure 12. Vertical Centerline Profiles at X/D =120; Case 2, Sc_t = 0.2.

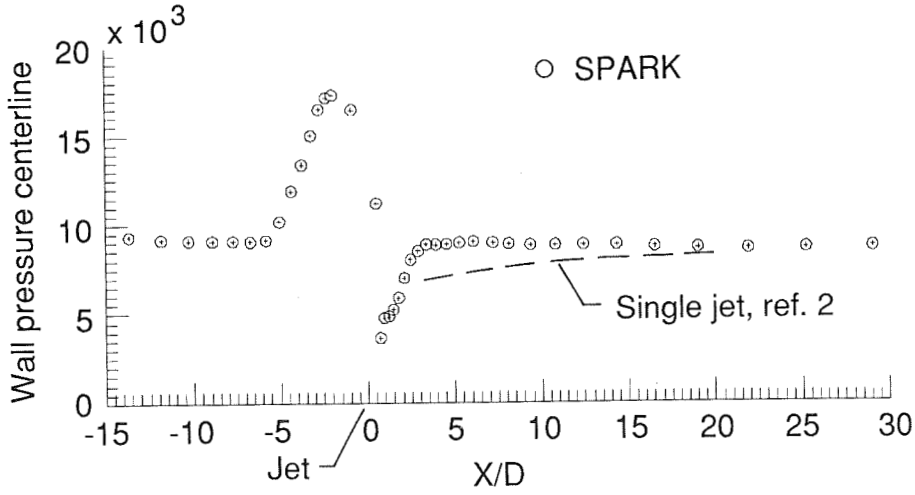

Figure 13. Longitudinal Centerline Wall Pressure; Case 2, Sc_t = 0.5.

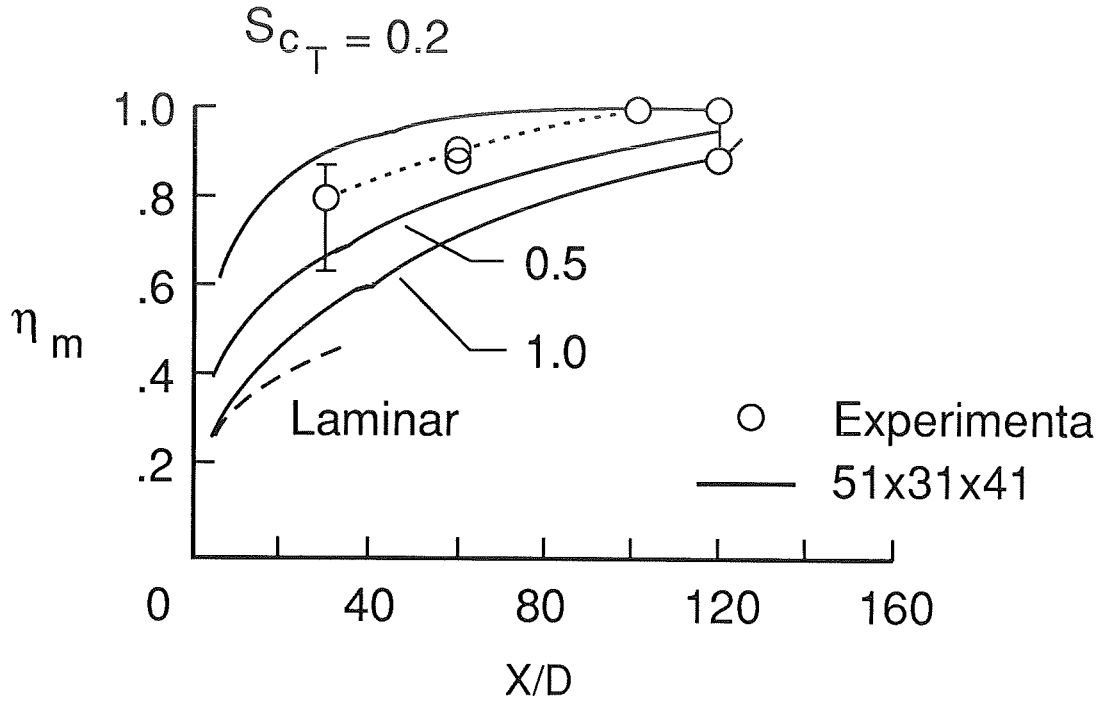

Figure 14. Fuel Mixing Efficiency Distribution; Case 2.

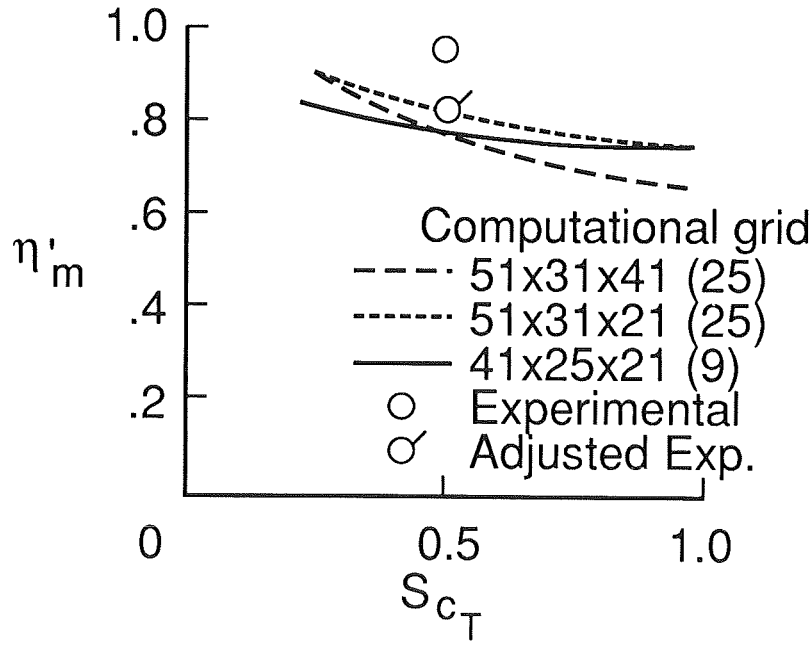

Figure 15. Fuel Mixing Efficiency at X/D = 120; Case 2.

Computed vertical jet centerline profiles (Sc_t = 0.2) at the 120D station are presented in Fig. 12 and compared with measured hydrogen mass fraction, static pressure, static temperature and velocity. Computed profiles are in excellent agreement with experimental results except for the fuel concentration. The magnitude of the peak computed hydrogen concentration is in excellent agreement with data but is offset to the wall. The dashed curve illustrates the computed H_2 mass fraction using Sc_t = 0.5. Peak concentration is about 80% higher than for the Sc_t = 0.2 solution.

Longitudinal jet centerline wall pressure distribution (Sc_t = 0.5) in the nearfield is illustrated in Fig. 13. These results show the extent of jet disturbance on upstream flow, recovery pressure in the upstream recirculation region, and low pressure in the wake downstream of the injector. Note that the pressure rise extends to 5.5D ahead of the injector, which is significantly greater than the "zero" hydrogen contour (α = .005) presented in Fig. 10a. Downstream pressure is in reasonable agreement with wall pressure data scaled from experiments in Ref. 2. Calculated results presented are closer to the injector than could be measured experimentally.

Calculated longitudinal distributions of mixing efficiency for Case 2 are illustrated in Fig. 14 for fine mesh solutions using Sc_t = 0.2, 0.5 and 1.0; and in Fig. 15 for all solutions at X/D = 120. Mixing efficiency presented in Fig. 14 is as defined by Eqn. 1; whereas the mixing efficiency presented in Fig. 15 was calculated using the incorrect value of stochiometric mass fraction presented by Eqn. 2. Experimental data presented on each figure have been adjusted to the appropriate definition. Fig. 14 illustrates the effect of turbulence on the mixing efficiency distribution. A laminar solution (Sc_t = 0.5) in the elliptic region illustrates that turbulence modeling is not an issue for the first 4 jet diameters downstream of the jet, as both the laminar and turbulent solutions have identical mixing efficiencies. However, Sc_t has a large impact in the downstream mixing, because it is used to determine the turbulent mass diffusivity from the turbulent viscosity. For Sc_t = 0.2, fuel mixing is complete (η_m = 1.0) at about X/D = 80, whereas experimental measurements indicate η_m reaches unity at about X/D = 100. Using Eqn. 3 to adjust mixing to account for all hydrogen injected produces flagged data points which are in better agreement with the Sc_t = 0.5 computational results. Between X/D = 5 and 30, turbulent mixing is about 50% higher than laminar mixing.

Figure 15 illustrates the effect of mesh density and turbulent Schmidt number on the fuel mixing efficiency η_m' at X/D = 120. Experimental points were obtained using Eqn. 1 and 2 to integrate data from Ref. 3. Adjusted data is from Eqn. 2 and 3 using data from Fig. 3 to determine the ratio of integrated total fuel to metered fuel flow rate. Fig. 15 illustrates the large impact of reduced turbulent Schmidt number on η_m' for fine grid solutions. Mixing efficiency is seen to increase from about 65% with Sc_t = 1.0 to 92% with Sc_t = 0.2. Coarse grids do not have as large a sensitivity to turbulent Schmidt number. Changing vertical mesh from 41 to 21 results in increased predicted mixing for Sc_t = 1.0 from 65% to 75% and no change for Sc_t = 0.2. The 41x25x21 mesh is coaser both in the x and y directions, as well as having the injector defined by 9 nodes versus 25 for the other cases, and the solutions are even less sensitive to Sc_t than other grids. Note that all solutions with Sc_t = 0.5 predict η_m = 0.79±0.04. Note also that the data is in the best agreement with fine grid solutions with Sc_t = 0.2 for this case.

Case 3

Only one computational solution was performed for the smallest normal jet, and results from that case are illustrated in Figures 16-18. The solution utilized a turbulent Schmidt

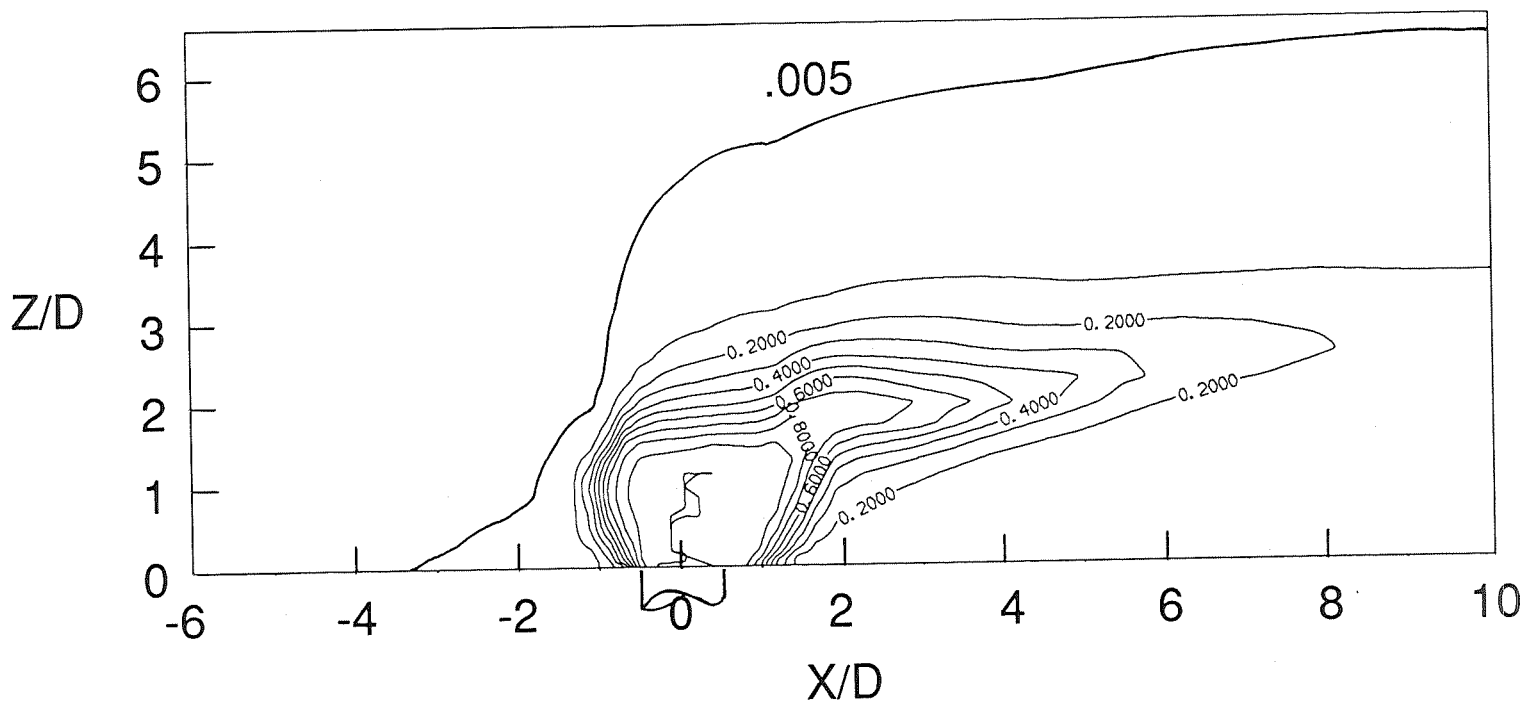

Figure 16. Longitudinal Hydrogen Mass Fraction Contours; Case 3, Sc_t = 0.2.

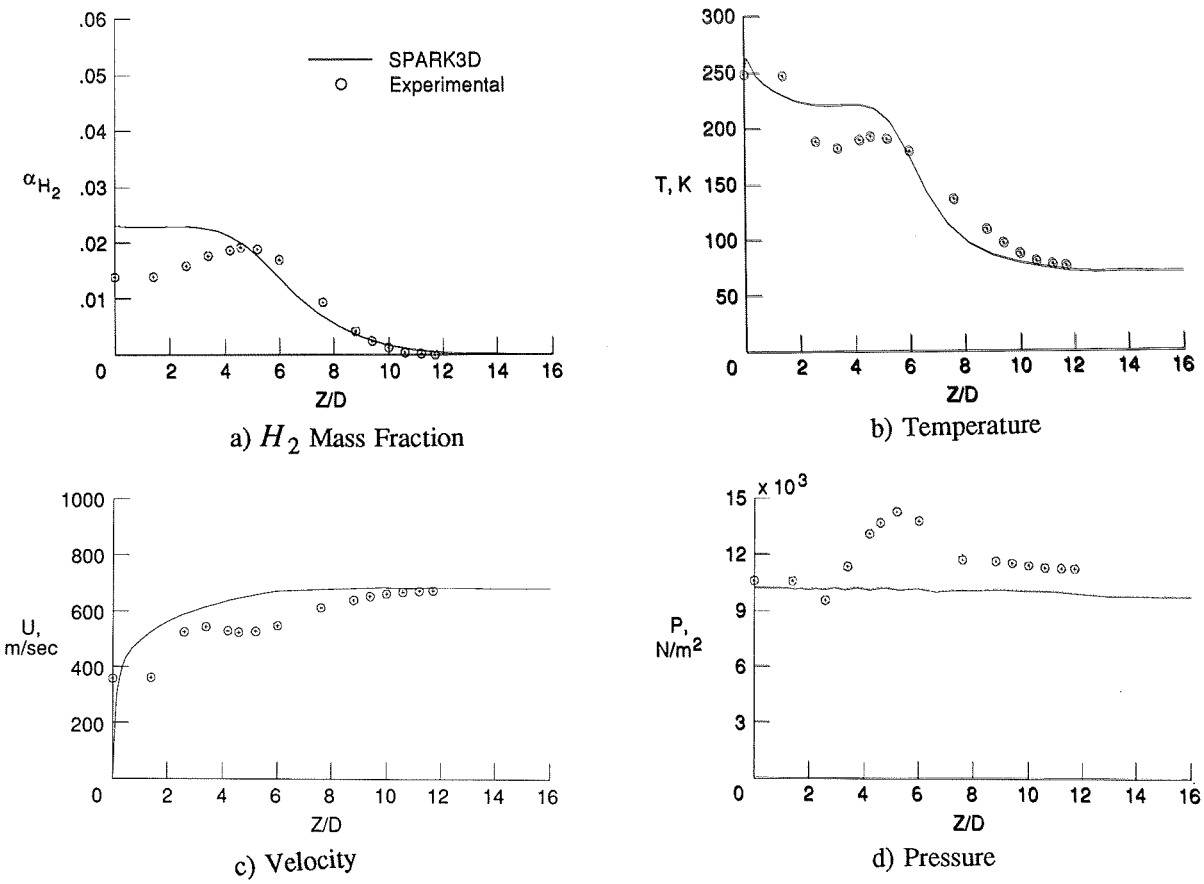

Figure 17. Vertical Centerline Profiles at X/D =120; Case 3, Sc_t = 0.2.

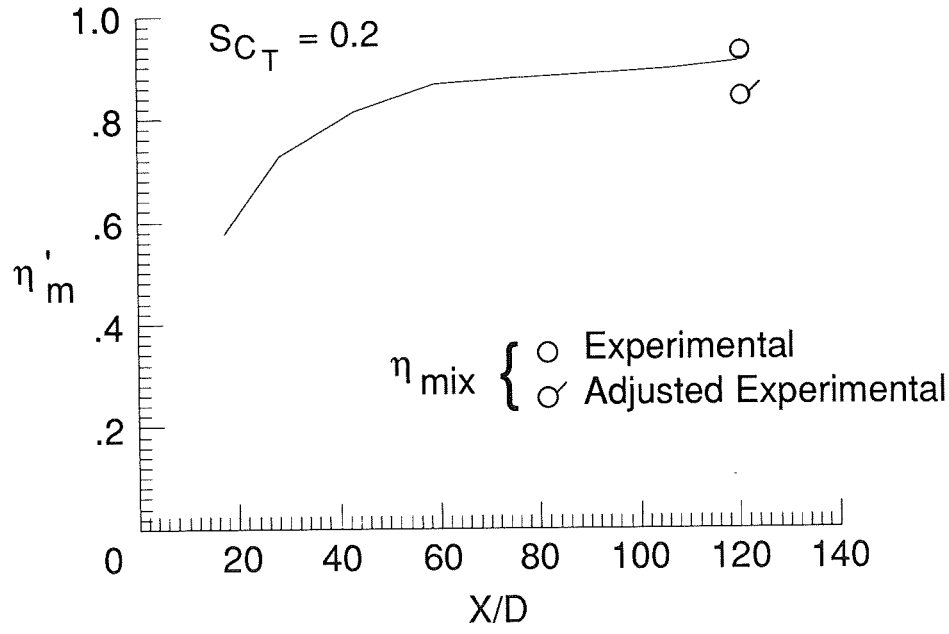

Figure 18. Fuel Mixing Efficiency Distribution; Case 3, Sc_t = 0.2.

number of 0.2.

Hydrogen contours presented in Fig. 16 illustrate fuel penetration, decay of the hydrogen core, and details of the upstream flow separation region. The 0.10 contour extends only about 1.1D upstream of the jet center, and the .005 contour extends about 3.2D upstream. The hydrogen core penetrates about 2.5D, and the 0.40 H_2 concentration persists only 5 jet diameters before dispersing.

Vertical jet centerline profiles at the 120D station are compared in Fig. 17 to experimentally measured values. In addition to the high fuel concentration at the wall for the computational results, the major differences arise from the variation in experimentally measured static pressure between 2 and 5 diameters from the wall. Because of the relative uniformity of the pressure for the other hydrogen cases, the pressure variations in the experimental data here are suspect. Notice the reasonable although slightly overpredicted maximum H_2 concentration and the extremely accurate agreement in the penetration of the .005 contour.

Computational mixing efficiency, η_m' defined in the nonstandard way discussed above (Eqn. 1 and 2) for Case 3 is compared with experimental results in Fig. 18. Whereas the correctly defined mixing efficiency is 100%, this nonstandard mixing efficiency actually allows quantitative comparison of two fully mixed results. Computational results using Sc_t = 0.2 underpredict the experimental mixing efficiency by 4% and over predict the adjusted mixing efficiency by 8%, consistent with predictions for Case 1 which had the thin boundary layer.

Case 4

Only one computational solution was obtained for the 30^o multiple hydrogen jets. The solution utilized a turbulent Schmidt number of 0.2, and results from that case are illustrated in Figures 19-21.

Hydrogen contours presented in Fig. 19 illustrate fuel penetration, decay of the hydrogen core, and details of the upstream flow separation region. The 0.10 contour extends about 2.0D upstream of the jet center, and the .005 contour extends about 2.5D upstream. The core penetrates about 2.0D, and the 0.40 H_2 concentration persists only 5.4 jet diameters before dispersing.

Vertical jet centerline profiles at the 120D station are compared in Fig. 20 to experimentally measured values. As with the cases from Ref. 4, the computed pressure underpredicts experimental values at the 120D station. Small differences in predicted and measured temperature and velocity are believed associated with boundary layer energization by the downstream angled fuel. Note that at Z/D = 2 the velocity is higher than the freestream value. Peak hydrogen mass fraction occurs at the wall for the computed flow, compared to about 3D above the wall for the data. The computed α_{max} is about 33% higher than experimental measurements. Based on results for Cases 1-3, this difference suggests that the predicted mixing efficiency for Sc_t = 0.2 is about 6% lower than the experimental values.

Longitudinal jet centerline wall pressure distribution in the nearfield is illustrated in Fig. 21. These results show the extent of the flow disturbance upstream of the injector and a very small low pressure region downstream of the injector. The pressure rise extends about 1D farther upstream than the .005 H_2 mass fraction contour. Unlike the Case 2 results, the downstream pressure increases following a low pressure region. This rise in pressure is believed to be associated with the multiple jet interacting bow shocks. Data at 3D on the jet centerline is

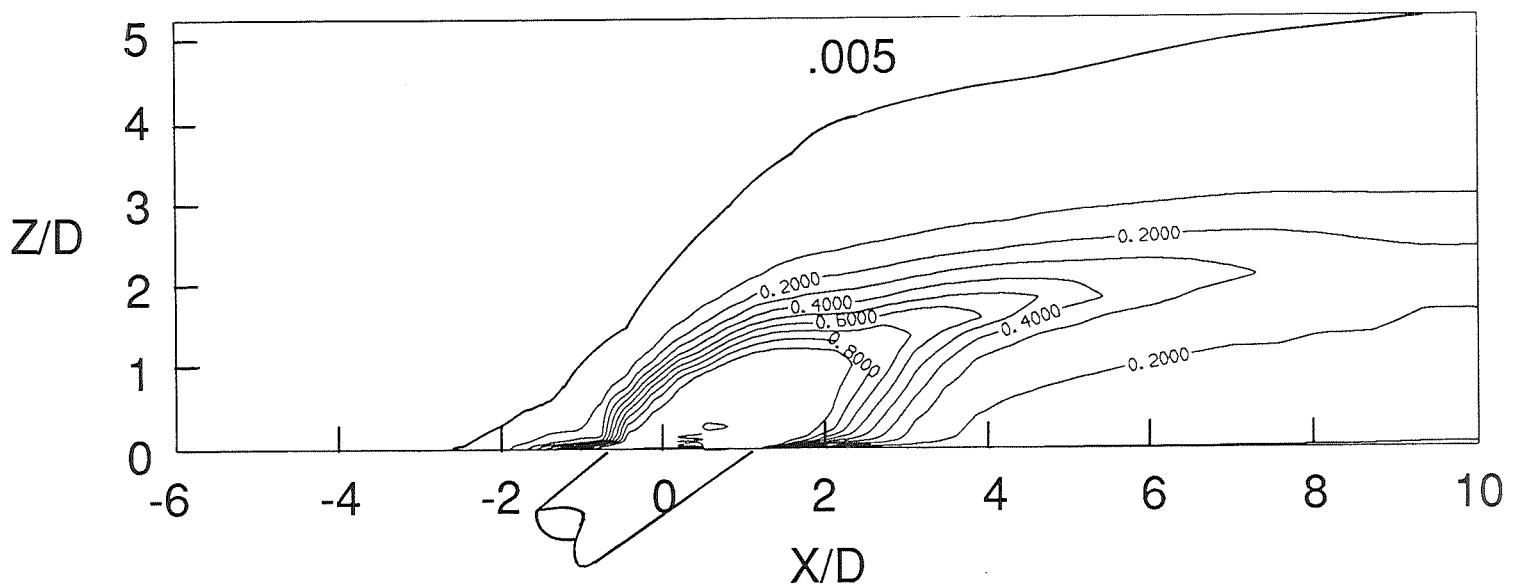

Figure 19. Longitudinal Hydrogen Mass Fraction Contours; Case 4, Sc_t = 0.2.

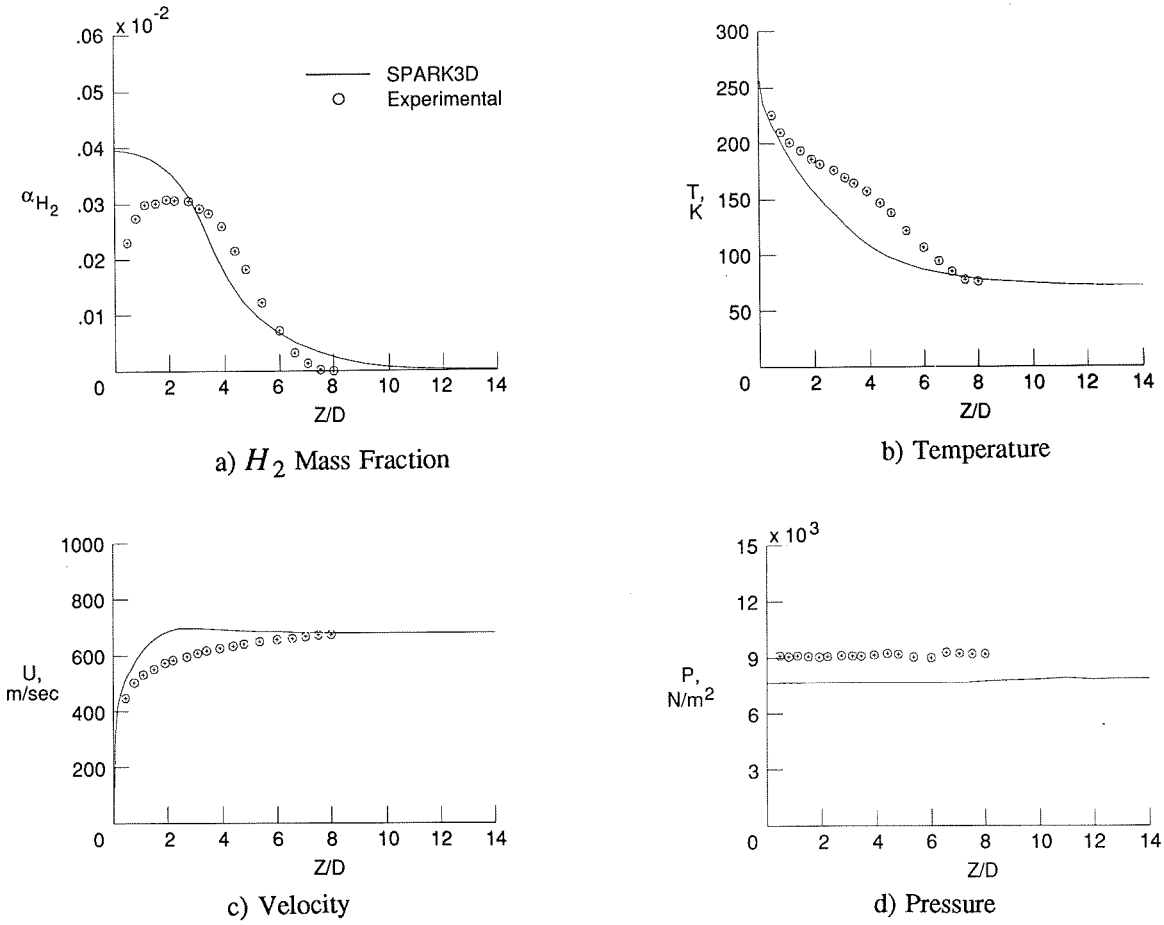

Figure 20. Vertical Centerline Profiles at X/D =120; Case 4, Sc_t = 0.2.

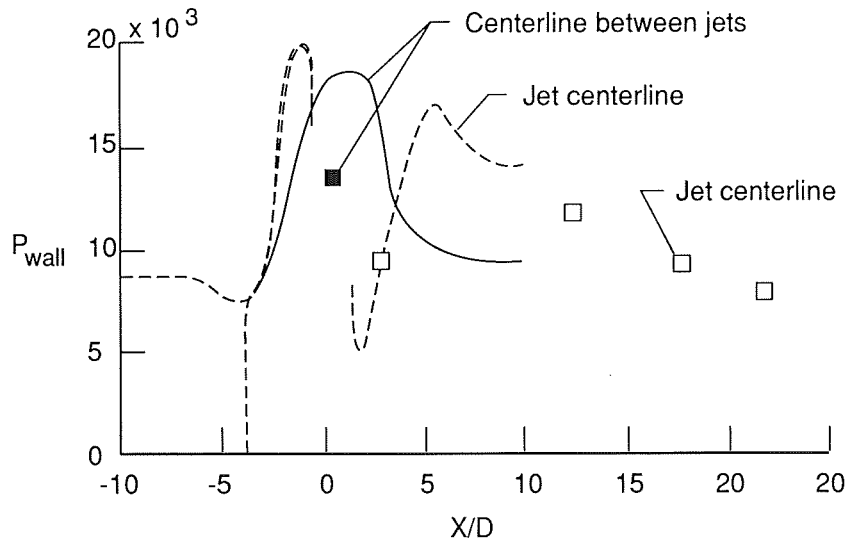

Figure 21. Longitudinal Centerline Wall Pressure; Case 4, Sc_t = 0.2.

in good agreement with prediction, however the data between jets is not.

Case 5

Only one computational solution was obtained for each of Cases 5 through 7. These solutions used Sc_t = 0.5, because that value provided excellent agreement with the experimental data. Comparisons of computational and experimental results for Case 5, 30^o matched static pressure helium injection, are presented in Figures 22-24.

Helium contours presented in Fig. 22 illustrate fuel penetration, decay of the core and details of the upstream flow separation. The .005 contour extends upstream only about 0.5D from the edge of the highly elongated angled injector. The He core penetrates about 1D off the wall, and the 0.40 contour extends downstream about 8D. Basically, the helium does not penetrate out of the boundary layer because of the low jet-to-freestream dynamic pressure ratio. Case 5 had a $\bar{q}$ of 0.6 versus 1.0 for the the 30^o injection of hydrogen in Case 4.

Vertical jet centerline mole fraction profiles at 20, 40 and 90 jet diameters are compared with experimentally measured values in Fig. 23. The nearfield core penetrates about 1.5D off the plate, but the outer edge of the mixing region remains within 4D, about half as high as data. In the farfield, a weak peak remains about 2D off the plate, unlike the H_2 cases. Peak concentration are in good agreement with data throughout.

Figure 24 presents longitudinal distributions of maximum helium mass fraction and penetration. Excellent agreement in the peak He concentration is illustrated in Fig. 24a, which was shown by the hydrogen cases to be a good indication that mixing efficiency is accurately predicted. Predicted helium penetration is quite low compared to data. Fig. 24b illustrates computed and experimental measurements of He penetration to the outer edge of the jet (x_{He} = 0.) and the to the location of peak concentration. Measured penetration of the edge is twice the computed value for the nearfield and about 25% higher than computed for the 90D station. However, the peak penetration is accurately modeled in the nearfield and only about 30% underpredicted at the 90D station.

Case 6

Comparisons of computational and experimental results for Case 6, 30^o underexpanded helium injection, are presented in Figures 25-27. This solution also utilized a Sc_t of 0.5.

Helium contours presented in Fig. 25 illustrate fuel penetration, decay of the core and details of the upstream flow separation. The .005 contour extends upstream about 1D from the edge of the highly elongated angled injector. The He core penetrates about 2.5D off the wall, and the 40% contour extends downstream past the end of the elliptic solution (>10D). Comparing Fig. 25 with Fig. 22, the underexpanded jet has much higher penetration, consistent with the fivefold increase in helium pressure and mass flow rate.

Vertical jet centerline mole fraction profiles at 20, 40 and 90 diameters are compared with experimentally measured values in Fig. 26. This high pressure jet penetrates about 4D off the plate in the nearfield, and the computational profile maintains a peak concentration 6D off the plate at the 90D station. Shape and magnitude of the x_{He} contours are in excellent agreement with experimental measurements at all three stations. The only noticible discrepancy is near the wall, where the experimental profile drops off more rapidly than the computational results.

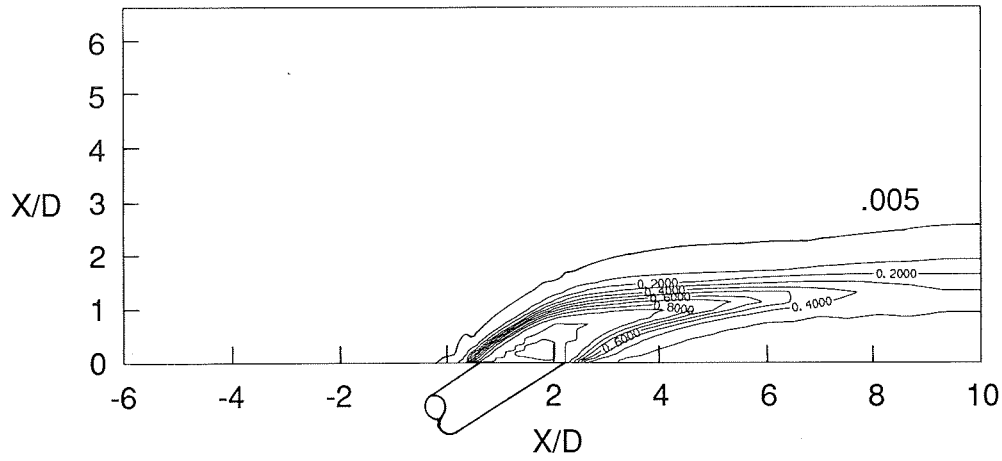

Figure 22. Longitudinal Helium Mass Fraction Contours; Case 5, $\theta = 30^o$, $\bar{q} = 0.6$.

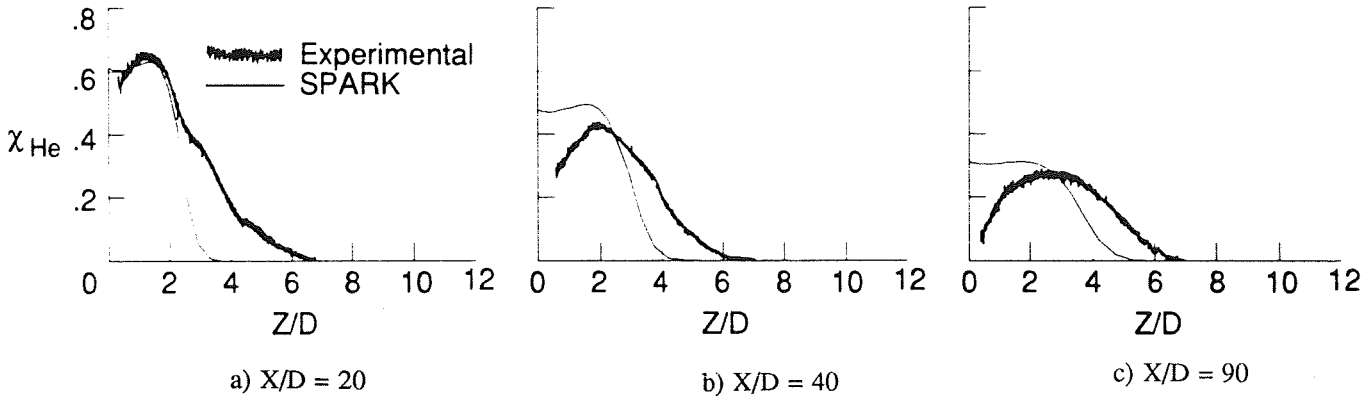

a) X/D = 20 b) X/D = 40 c) X/D = 90

Figure 23. Vertical Centerline Helium Mole Fraction Profiles; Case 5, $\theta = 30^o$, $\bar{q} = 0.6$.

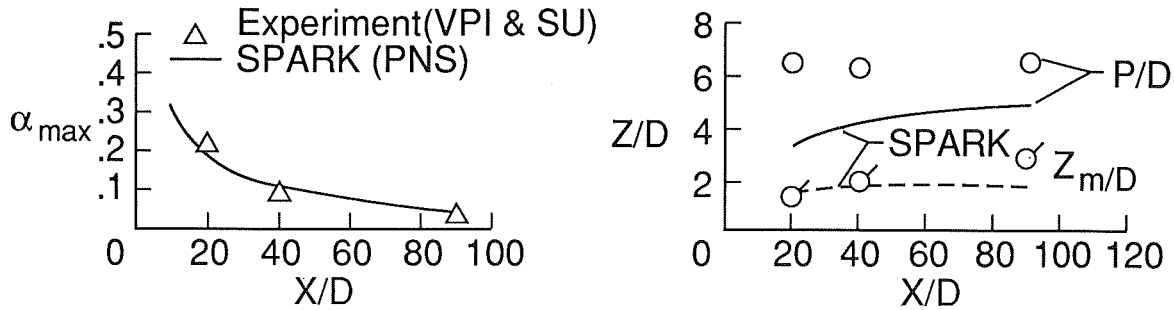

a) Maximum Helium Mass Fraction b) Helium Penetration

Figure 24. Longitudinal Distributions; Case 5, $\theta = 30^o$, $\bar{q} = 0.6$.

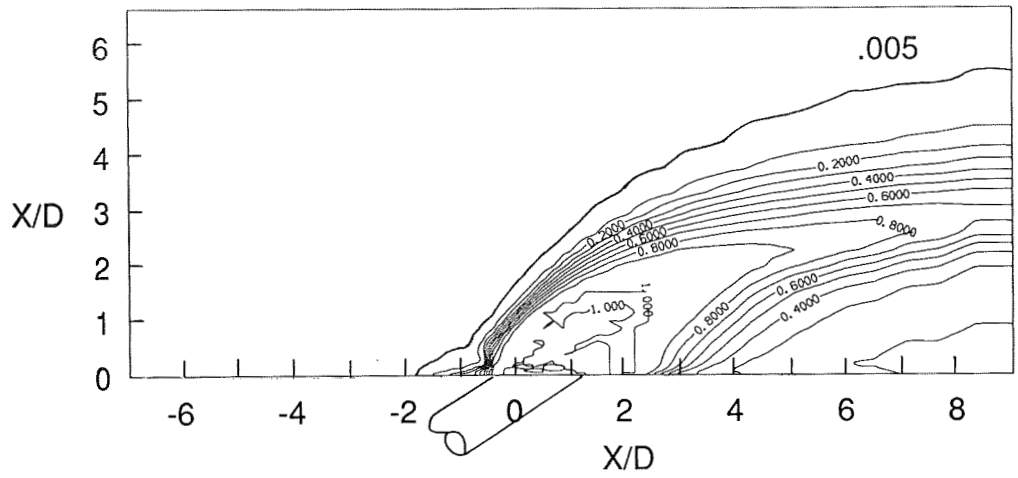

Figure 25. Longitudinal Helium Mass Fraction Contours; Case 6, $\theta = 30^o$, $\bar{q} = 3.1$.

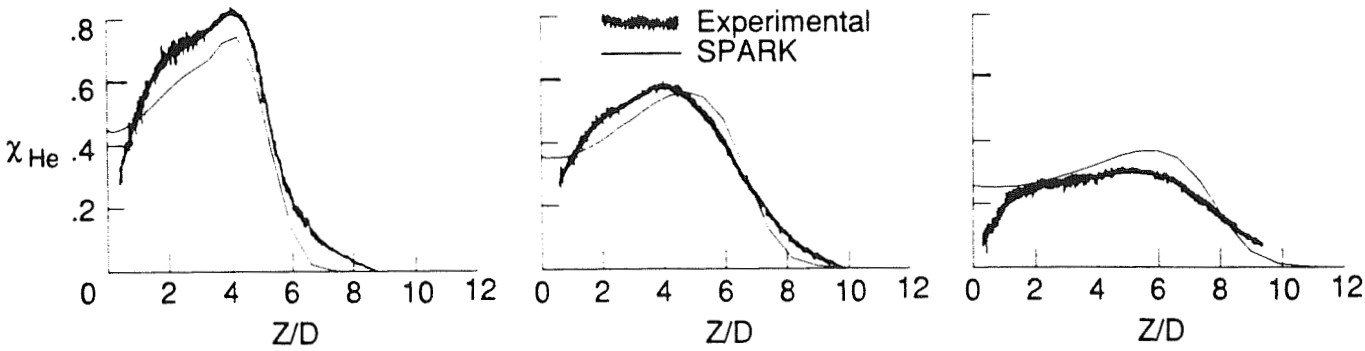

a) X/D = 20 b) X/D = 40 c) X/D = 90

Figure 26. Vertical Centerline Helium Mole Fraction Profiles; Case 6, $\theta = 30^o$, $\bar{q} = 3.1$.

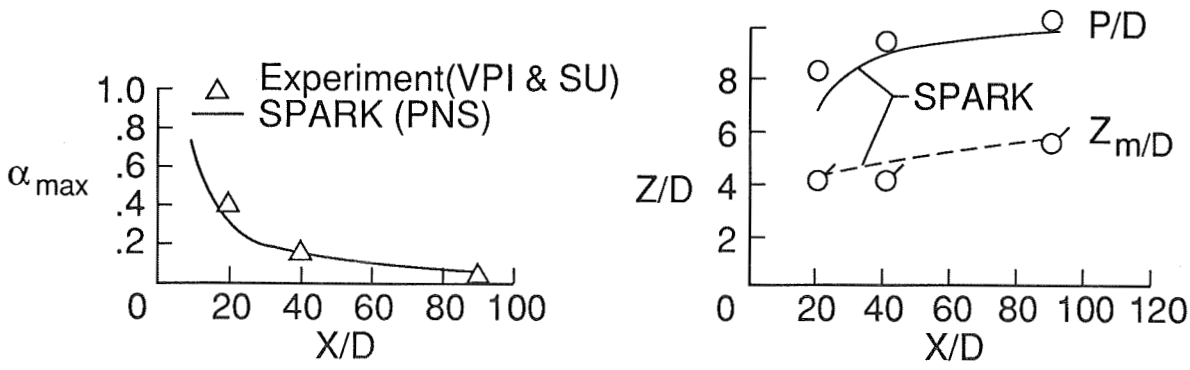

a) Maximum Helium Mass Fraction b) Helium Penetration

Figure 27. Longitudinal Distributions; Case 6, $\theta = 30^o$, $\bar{q} = 3.1$.

Figure 27 presents longitudinal distribution of maximum helium mass fraction α_{max} and penetration P/D. The excellent agreement in Fig. 27a indicates that mixing efficiency is accurately predicted. Computed helium penetration, both core and outer edge of mixing region, are compared to experimental results in Fig. 27b and show excellent agreement. The largest discrepancy is the 15% underpredicted penetration of the edge at X/D = 20.

Case 7

Comparisons of computational (Sc_t = 0.5) and experimental results for Case 7, 15° matched static pressure injection, are presented in Figures 28-30.

Helium contours presented in Fig. 28 illustrate fuel penetration, decay of the core and details of the upstream flow separation. The .005 contour extends upstream about 0.5D from the edge of the highly elongated angled injector. The He core penetrates about 0.5D off the wall, and the 40% contour extends downstream about 10D.

The low pressure, low angle injector produces a mixing region characterized by the highest He concentration and core on the wall by the first survey station, X/D =20, as illustrated by the vertical profiles in Fig. 29. The computational results indicate that a core exists off the wall in the nearfield, but returns to the wall by the 20D station. Shape and magnitude of the predicted mole fraction contours are in good agreement with experimental contours. However, the underprediction of the peak x_{He} by about 40% at the 90D station suggests that a slightly lower value of Sc_t may be appropriate for this case. However, this is inconclusive, since the experimental data for this case showed an unexplained asymmetry.

Figure 30 presents longitudinal distribution of maximum helium mass fraction α_{max} and penetration P/D. Fig. 30a illustrates good agreement between calculated and measured peak helium mass fraction, suggesting that the computational results accurately predict mixing efficiency. Predicted helium penetration to the outer edge of the mixing region is compared to the experimental data in Fig. 30b, illustrating slight underprediction at 20 and 40 X/D, but excellent agreement at the 90D station.

DISCUSSION OF RESULTS

Qualitatively, the computations are good in that computational trends are consistent with experimental observations. The results show that increasing δ/D increases penetration, both of the outer edge of the mixing region and of the point of maximum concentration, which was a conclusion of Ref. 4. Pressure plots (not included) reveal bow shocks which are naturally stronger for the normal injection and underexpanded injection. Velocity vector plots (also not included) reveal the horseshoe vortex system characteristic of injection flow fields. These and other observations and details of the flow solutions are beyond the scope of this presentation, but will be addressed in the future.

Accuracy

Table 4 summarizes observed differences between computed and experimental measurements for jet penetration (P/D and Z_m/D), spreading (W/D and W_B/D), maximum H_2 concentration (α_{max}), and mixing efficiency, η_m.

Where available, solutions using Sc_t = 0.5 as recommended above are included in the table. Because of the recognized errors in the hydrogen data, the Sc_t = 0.2 solutions are used

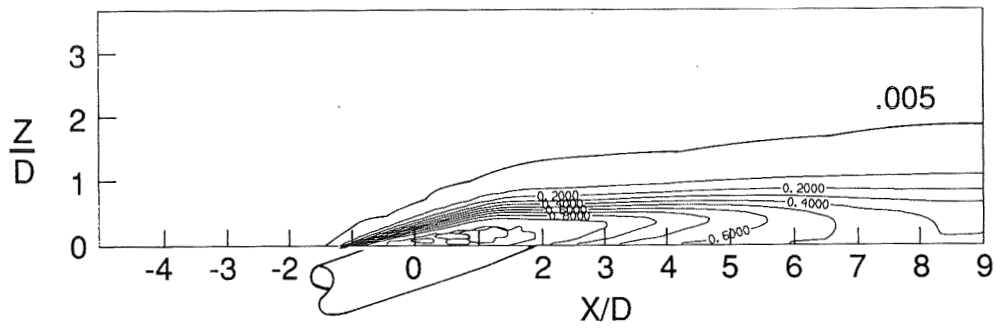

Figure 28. Longitudinal Helium Mass Fraction Contours; Case 7, $\theta = 15^o$, $\bar{q} = 0.27$.

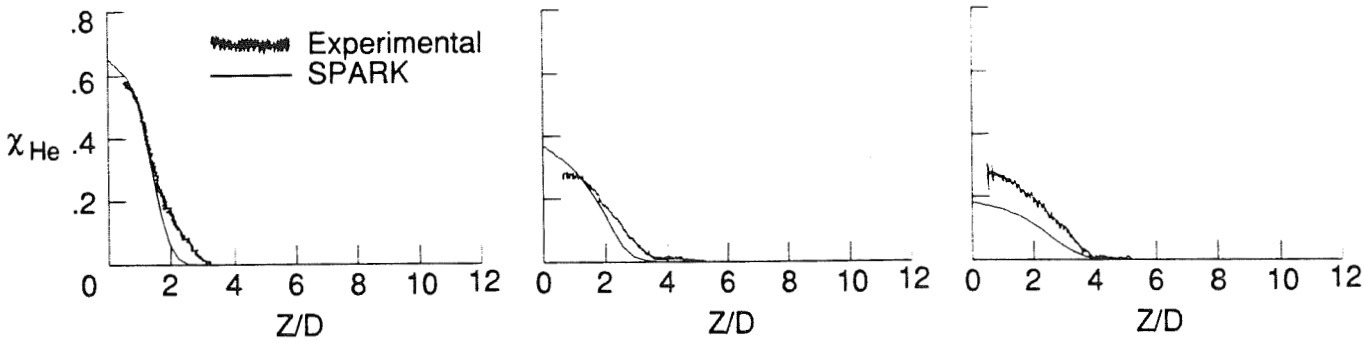

a) X/D = 20 b) X/D = 40 c) X/D = 90

Figure 29. Vertical Centerline Helium Mole Fraction Profiles; Case 7, $\theta = 15^o$, $\bar{q} = 0.27$.

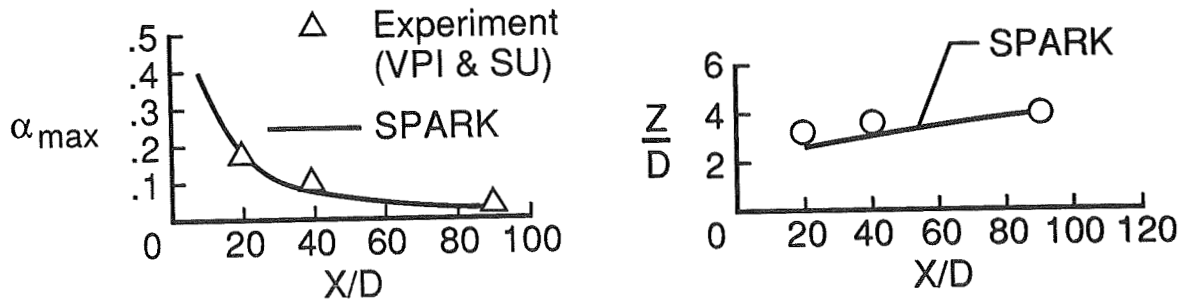

a) Maximum Helium Mass Fraction b) Helium Penetration

Figure 30. Longitudinal Distributions; Case 7, $\theta = 15^o$, $\bar{q} = 0.27$.

when comparing peak hydrogen mass fraction and mixing efficiency. Mean deviation is summarized in the last column.

The codes consistently underpredicted penetration of the maximum concentration (Z_m/D) in the farfield, generally leaving the peak along the wall. Penetration to the outer edge of the mixing layer is generally predicted within ±1.6 diameters, or to within about ±7%.

Lateral spreading is slightly overpredicted in the freestream and generally significantly overpredicted in the boundary layer. Comparisons available are insufficient to provide reliable estimates, but the range is about 1D for W and -2D for W_B.

Peak injectant concentration in the farfield is over or underpredicted by about ±17%, while the unadjusted fuel mixing efficiency has an average deviation of 5% (universally underpredicted). Confidence in this mixing efficiency accuracy will be significantly enhanced by additional data and integration of the available helium data.

Table 4. Accuracy Summary

Case no.	1	2	3	4	5	6	7	M.D.
X/D	120	120	120	120	90	90	90	
Sc_t	0.2	0.5	0.2	0.2	0.5	0.5	0.5	
P/D	2.0	4.0	0.0	3.0	-1.8	-0.5	0	1.6
Z_m/D	-2.5	-3.0	-2.5	-2.5	-1.5	0.2	0	1.7
W/D	1.25	.70	--	--	--	--	--	.98
W_B/D	4.0	0.2	--	--	--	--	--	2.1
α_{max}	-14%	0%*	20%	30%	10%	12%	-30%	17%
η_m	-.09	−.05*	-.03	--	--	--	--	.05

* Sc_t = 0.2

Recommendations

There are obvious differences between the hydrogen and helium cases in the application of the code to achieve acceptable code vs. experiment agreement. For the H_2 cases, better agreement was obtained using Sc_t = 0.2, whereas for the He cases, better agreement was obtained with Sc_t = 0.5. Because of the superior experimental measurement capability of the recent helium tests reported in Ref. 30 and documented uncertainties of the older hydrogen data[3,4 and 7], it is prudent to recommend solution techniques used for Cases 5-7. Therefore, when using a fine grid and the Baldwin-Lomax turbulence model, results indicate that mixing of transverse injectors with injection angles, between 15 and 90 degrees should be modeled using $Sc_t \approx$ 0.5. However, when performing a complete combustor analysis requiring a coarse grid with multiple fuel injectors, a more realistic prediction of fuel mixing may be achieved using Sc_t = 1.0[28]. It would also be advisable to compare grid density used for such solutions to the injection cases (preferably He) presented in this paper.

Fuel mixing efficiency is relatively insensitive to maximum fuel concentration (Cases 1 and 2). If the decay of peak fuel concentration is accurately predicted, then the mixing efficiency will be accurate, but not vice versa.

Turbulent diffusivity (Schmidt number) has been shown to vary across a boundary layer[37] and that trend appears in Table 4. Lateral spreading within and spreading out of a boundary layer are not correctly predicted when using a single value of Sc_t over the entire flow. This observation suggests that improved turbulence modeling to account for the nonuniform turbulent diffusivity is in order.

CONCLUSIONS

The SPARK family of Navier Stokes codes were validated for fuel mixing in a supersonic flow, using experimental data for discrete circular injectors angled at 15^o (downstream) to 90^o (normal) for air flow boundary layer thicknesses ranging from 1.25 to 6.25 injector diameters. Details of the physical model, solution methodology, boundary conditions and turbulence model are presented in sufficient detail such that recreation of the solutions is possible. Results presented demonstrate that "grid converged" solutions for one injector were not attained but that mixing efficiency sensitivity is acceptable. Mixing efficiency is also relatively insensitive to peak fuel concentrations. Recommendations are presented for modeling the fuel injector problem. These recommendations are different depending on the grid density around each injector. Coarse grids require damped turbulence (achieved with a turbulent Schmidt number of unity). This type of grid is representative of large scale combustor solutions with many fuel injectors. Fine grids require a reduced turbulent Schmidt number on the order of 0.5, which are in agreement with experimentally observed values for similar flows. The turbulent Schmidt number is not constant across the entire flow domain; a distribution may enhance fuel injection modeling.

REFERENCES

1 Northam, G.B. and Anderson, G.Y., "Supersonic Combustion Ramjet Research at Langley," AIAA Paper 86-0159, presented at 24th Aerospace Sciences Meeting, Reno, NV.

2 Torrence, M.G., "Concentration Measurements of an Injected Gas in a Supersonic Stream," NASA TN D-3860, 1967.

3 Rogers, R.C., "A Study of the Mixing of Hydrogen Injected Normal to a Supersonic Airstream," NASA TN D-6114, 1971.

4 McClinton, C.R., "Effect of Ratio of Wall Boundary-Layer Thickness to Jet Diameter on Mixing of a Normal Hydrogen Jet in a Supersonic Stream," NASA TM X-3030, 1974.

5 Orth, R.C., Schetz, J.A. and Billig, F.S., "The Interaction and Penetration of Gaseous Jets in Supersonic Flow," NASA CR-186, 1969.

6 Rogers, R.C., "Mixing of Hydrogen Injected From Multiple Injectors Normal to a Supersonic Airstream," NASA TN D-6476, 1971.

7 McClinton, C.R., "The Effect of Injection Angle on the Interaction Between Sonic Secondary Jets and a Supersonic Free Stream," NASA TN D-6669, Feb. 1972.

8 Anderson, G.Y. and Vick, A.R., "An Experimental Study of Flame Propagation in Supersonic Premixed Flows of Hydrogen and Air," NASA TN D-4631, June 1968.

9 Beach, H.L., Jr., "Supersonic Mixing and Combustion of a Hydrogen Jet in a Coaxial High-Temperature Test Gas," AIAA Paper 72-1179, Nov.-Dec. 1972.

10 Rogers, R.C. and Eggers, J.M., "Supersonic Combustion of Hydrogen Injected Perpendicular to a Ducted Vitiated Airstream," AIAA Paper 73-1322, Nov. 1973.

11 Anderson, G.Y. and Gooderum, P.B., "Exploratory Tests of Two Strut Fuel Injectors for Supersonic Combustion," NASA TN D-7581, 1974.

12 Rogers, R.C., "Influence of Fuel Temperature on Supersonic Mixing and Combustion of Hydrogen," AIAA Paper 77-17, 1977.

13 Eggars, J.M., Reagon, P.G. and Gooderum, P.B., "Combustion of Hydrogen in a Two-Dimensional Duct With Step Fuel Injectors," NASA TP-1159, 1978.

14 McClinton, C.R. and Gooderum, P.B., "Direct-Connect Test of a Hydrogen-Fueled Three-Strut Injector for an Integrated Modular Scramjet Engine," 14th JANNAF Combustion Meeting, Vol. II, CPIA Publ. 292, 489-505, Dec. 1977.

15 McClinton, C.R., "Interaction Between Step Fuel Injectors on Opposite Walls in a Supersonic Combustor Model," NASA TP-1174, 1978.

16 Northam, G.B., Trexler, C.A. and Anderson, G.Y., "Characterization of a Swept-Strut Hydrogen Fuel-Injector for Scramjet Applications," 15th JANNAF Combustion Meeting, Vol. III, CPIA Publ. 297, 393-410, Feb. 1979.

17 Anderson, G.Y. and Rogers, R.C., "A Comparison of Experimental Supersonic Combustor Performance with an Empirical Correlation of Nonreactive Mixing Results," NASA TM X-2429, Oct. 1971.

18 Guy, R.W. and Mackley, E.A., "Initial Wind Tunnel Tests at Mach 4 and 7 of a Hydrogen-Burning, Airframe-Integrated Scramjet," NASA Paper 79-8045, presented at the 4th International Symposium on Air Breathing Engines (Lake Buena Vista, FL), Apr. 1979.

19 Drummond, J.P., Rogers, R.C. and Evans, J.S., "Combustor Modeling For Scramjet Engines," AGARD 54th (B) Specialists Meeting On Combustor Modeling, Propulsion, and Energetics Panel, Cologne, Germany, Oct. 1979.

20 Pan, Y.S., Drummond, J.P. and McClinton, C.R., "Comparison of Two Computer Programs by Predicting Turbulent Mixing of Helium in a Ducted Supersonic Airstream," NASA TP-1166, May 1978.

21 Evans, J.S., Schexnayder, C.J., Jr. and Beach, H.L., Jr., "Application of a Two-Dimensional Parabolic Computer Program to Prediction of Turbulent Reacting Flows," NASA TP-1169, Mar. 1978.

22 Rogers, R.C. and Weidner, E.H., "Analysis of Hydrogen Combustion in High Enthalpy Supersonic Air Flows From a Shock Tunnel," 23rd JANNAF Combustion Meeting, Vol. III, CPIA Publ. 457, Oct. 1986.

23 Rogers, R.C. and Chinitz, W., "On the Use of a Global Hydrogen-Air Combustion Model in the Calculation of Turbulent Reacting Flows," AIAA Paper 82-0112, Jan. 1982.

24 Chinitz, W., "Theoretical Studies of the Ignition and Combustion of Silane-Hydrogen-Air Mixtures," NASA CR-3876, Feb. 1985.

25 Uenishi, K. and Rogers, R.C., "Three-Dimensional Computations of Mixing of Transverse Injector in a Ducted Supersonic Airstream," AIAA Paper 86-1423, Huntsville, AL, June 1986.

26 Uenishi, K., Rogers, R.C., and Northam G.B., "Three-Dimensional Computation of Transverse Hydrogen Jet Combustion in a Supersonic Airstream," AIAA Paper 87-0089, Reno, NV, Jan. 1989.

27 Chitsomboon, T., Northam, G.B., Rogers, R.C. and Diskin, G.S., "CFD Prediction of the Reacting Flowfield Inside a Subscale Scramjet Combustor," AIAA Paper 88-3259, Boston, MA, July 1988.

28 Srinivasan, S., Kamath, P. and McClinton, C.R., "Numerical Simulation of Flow Through the Langley Parametric Scramjet Engine," SAE Paper 892314, Los Angeles, CA, Sept. 1989.

29 Riggins, D.W., Mekkes, G.L., McClinton, C.R. and Drummond, J.P., "A Numerical Study of Mixing Enhancement in a Supersonic Combustor," AIAA Paper 90-0203, Jan. 1990.

30 Mays, R.B., Thomas, R.H. and Schetz, J.A., "Low Angle Injection Into a Supersonic Flow," AIAA Paper 89-2461, Monterey, CA, July 1989.

31 Ng. W.F., Kwok, F.T. and Ninnemann, T.A., "A Concentration Probe for the Study of Mixing in Supersonic Shear Flows," AIAA 89-2459, Monterey, CA, July 1989.

32 Drummond, J.P., Rogers, R.C. and Hussaini, M.Y., "A Detailed Numerical Model of a Supersonic Reacting Mixing Layer," AIAA Paper 86-1427, June 1986.

33 Carpenter, M.H., "Three-Dimensional Computations of Cross-Flow Injection and Combustion in a Supersonic Flow," AIAA Paper 89-1870, June 1989.

34 Kamath, H., "Parabolized Navier-Stokes Algorithm for Chemically Reacting Flows," AIAA Paper 89-0386, Jan. 1989.

35 Baldwin, B. and Lomax, H., "Thin Layer Approximation and Algebraic Model for Separated Turbulent Flows," AIAA Paper 78-257, 1978.

36 Sturgess, G.J. and McManus, K.R., "Calculations of Turbulent Mass Transport in a Bluff-Body Diffusion-Flame Combustor," AIAA Paper 84-0372, Jan. 1984.

37 Launder, B.E. and Spaulding, D.B., *Mathematic Models of Turbulence*, Academic Press, 1972, p. 49.